A NETWORK-CELL BASED FRAMEWORK FOR MULTISCALE ANALYSIS OF GRANULAR MATERIALS

By

JAGAN MOHAN PADBIDRI

A dissertation submitted in partial fulfillment of
the requirements for the degree of

DOCTOR OF PHILOSOPHY

WASHINGTON STATE UNIVERSITY
School of Mechanical and Materials Engineering

May 2010

To the Faculty of Washington State University:

The members of the Committee appointed to examine the dissertation of JAGAN MOHAN PADBIDRI find it satisfactory and recommend that it be accepted.

_____

Sinisa Dj. Mesarovic, Ph.D., Chair

_____

Alexander Panchenko, Ph.D.

_____

Balasingam Muhunthan, Ph.D.

_____

Hussein M. Zbib, Ph.D.

ACKNOWLEDGEMENTS

I would like to thank my committee chair and advisor Dr. Sinisa Mesarovic under whose guidance this research was conducted. He is a model advisor and a critical researcher. He has always allowed me to approach problems independently, at the same time providing useful feedback. I have learnt a great deal about critical thinking from him. He has constantly supported me even in times of personal adversity. I shall always owe him a debt of gratitude. I would also like to thank my other committee members Drs. Balasingam Muhunthan, Hussein Zbib and Alexander Panchenko for being in my committee and providing helpful suggestions. I would like to thank Ms. Carly Hansen for contributing to my research under the REU program.

I would also like to thank all my friends in Pullman, especially Raghu Baskaran, Harish Radhakrishnan and Prabhakar Singh who have always supported and encouraged me. I would also like to acknowledge the financial support received from the School of Mechanical and Materials Engineering, WSU and US DOE/MICS, Grant # DE-FG02-05ER25709 for the completion of my degree. Above all, I would like to thank my parents and my brother for encouraging me.

.

A NETWORK-CELL BASED FRAMEWORK FOR MULTISCALE ANALYSIS OF GRANULAR MATERIALS

Abstract

by Jagan Mohan Padbidri, Ph. D.
Washington State University
May 2010

Chair: Sinisa Dj. Mesarovic

This dissertation explores the numerical tools used for computer simulations and the qualitative micromechanics of granular materials. The discrete element method is an invaluable tool for studying the complex behavior of heterogeneous media like granular matter. Its main shortcoming is its computational intensity, arising from vast difference between the observation and the integration timescales which is particularly acute for macroscopically quasistatic deformation processes.

We first define macroscopically quasistatic processes, on the basis of dimensional analysis. This sets bounds for application of commonly used method for computational acceleration - superficially increased mass of particles. The dimensional analysis of the governing equations also motivates the separation of timescales for the integration of rotations and translations. Take advantage of the difference in characteristic timescales, we develop a two-timescales algorithm based on the concept of inertial manifolds. The algorithm is tested on a biaxial simulation and benchmarked against the accurate short-time step simulation which confirms its accuracy.

We then address the effect of boundary conditions on the deformation of granular material using numerical simulations. Three different boundary conditions are used to simulate

biaxial compression: 1) by prescribing a membrane, 2) by imposing pressure directly on the particles and strain for both cases using rigid plates and 3) by prescribing a penalty function which imposes only strain without the rigid boundary effects. Typically observed properties like persistent shear localization are shown to be an effect of the rigid plates. The effect of the membrane stiffness is examined. The penalty method is shown to yield more uniform stress distributions. Further, the penalty method induces *slip bands* where deformation localizes, but does not persist in the absence of rigid boundaries.

Granular materials display strain localization as shear bands accompanied by massive rolling. The propagation of rotations, which is closely related to the shear band width, has not been addressed previously. Using numerical techniques, we investigate the effect of force chains on rotation propagation. The transmission of rotations is found to depend on the force network strength and the length scale of the transmissions describes the width of a typical shear band in these materials.

TABLE OF CONTENTS

LIST OF FIGURES

LIST OF TABLES

DEDICATION

I dedicate this work to my parents, Dr. Raghuveer Rao Padbidri and Dr. Bhaskaram Padbidri and to my loving brother, Prashanth Madhav Padbidri. None of this would have been possible without you.

1. Introduction

Granular media exhibit a set of complex behaviors, which separates them from conventional engineering materials, like dilatancy and almost always, strain localization in the form of shear bands. It is also well known that the distribution of forces in a granular medium is uneven (Fig. 1.1), initially observed experimentally by Drescher A and De Josselin De Jong [1]. The assembly of particles organizes in such a way that the bulk of the load is carried by a relatively small number of particles which orient themselves in the form of force chains. The distribution of forces, though non-uniform, is structured, which enables the assembly of particles to bear the load [2]. Statistical studies indicate that roughly 60% of the particles are subject to forces lesser than the average force applied on the assembly and that the number of force chains carrying greater than average forces decreases exponentially as the magnitude of the forces increase [3].

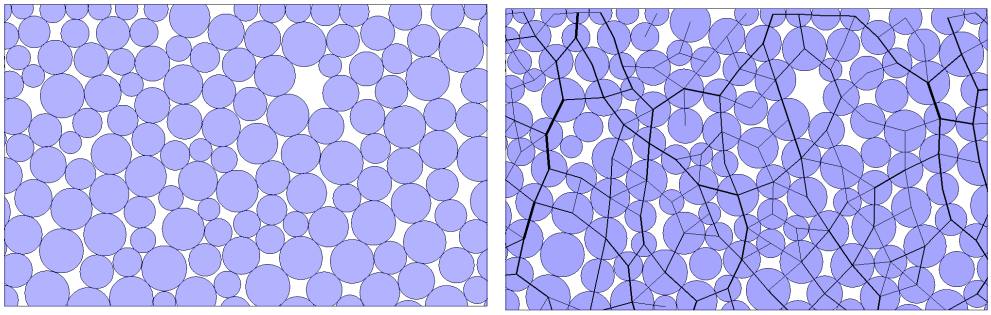

Figure 1.1. The heterogeneity of granular structure and the resultant uneven distribution of forces

The reason for these behaviors can be attributed to the nature of composition of these materials. Granular materials are composed of distinct particles, which interact with each other only at mutual contact points. The discontinuous character of the medium results in the aforementioned behaviors and implies that deformation of the medium does not always imply deformation of the particles, but signifies their topological rearrangement. Individual particles

are deformed though, in high pressure processes like powder compaction and sintering. As the granular material deforms, force chains still exist. However, the structure formed by the interconnected force chains is not necessarily stable. The instabilities of the force chain network promote the rearrangement of the particles into a more stable configuration. The instabilities in the force chains do not occur on a global scale i.e. at any given instant, a deforming granular material contains parts of the assembly where the force chains are stable and do not promote particle rearrangement and parts of the assembly where local instabilities cause particle rearrangement. This implies that some part of the deforming granular material 'flows' while a large part of it stays intact and moves as a rigid object [4].

Another interesting property of granular materials is dilatancy. Dilatancy is the phenomenon of increase in bulk of a material when subjected to change of shape, in the form of an imposed shear stress. The micro-mechanics that govern this observation are simple. When a granular material is sheared, under low pressure, the particles have to move over one another since the forces due to the pressure are not large enough for the particles to deform each other. This mechanism contributes to the increase in volume as the material shears. As the shear deformation progresses, the material expends its capacity to dilate, reaching a critical state, which is characterized by fluid like flow. The extent to which a granular material dilates depends on its initial volume density. The existence of critical volume fraction corresponding to the critical state was recently demonstrated using numerical simulations [5].

The research for this dissertation is confined to low pressure, quasistatic deformation of granular materials which is of primary interest to geomechanicians. The most common method

used to understand granular deformation in this regime is through biaxial and triaxial experiments, which are the methods being investigated here. Despite significant advances made to understand this deformation regime, some critical questions remain unanswered. This work is intended to address some of those issues through numerical experiments. The basics of the numerical technique will be introduced first followed by the specific problems being addressed.

Computational methods provide a convenient way to investigate the evolution of deformation on an individual particle level. The Discrete Element Method was developed specifically for this class of problems by Cundall and Strack [6]. Following this, numerous researchers, [2, 7 – 12] have implemented the idea for various investigations and also using different interpretations. The method treats each particle as an independent entity. Due to this, the average number of inter-particle contacts (co-ordination number), distributions of displacement and velocity vectors of each particle of the assembly can be easily captured, features which are difficult to investigate experimentally. The method ignores the deformation of an individual particle. Despite this, DEM has been instrumental in providing some insightful information on the micromechanics of granular materials, for e.g. Oda and Kazama [13] noticed in their experiments that creation of voids and rotation of particles were hallmarks of strain localization. Numerical results conform to this observation [9]. These observations indicate that rolling of particles plays a prominent role in the deformation process though the sliding of particles over each other was traditionally well accepted in this field of research.

The Discrete Element Method, abbreviated as DEM, is essentially a particle dynamics method which integrates Newton's second law of motion in time to trace the trajectory of each

particle. The total force on each particle is the sum of forces arising from all its contacts and the imposed boundary forces. The DEM uses an explicit time integration scheme to solve the equations of motion for each particle for finite time increments. The updated positions of the particles and boundaries are used to update the set of contacts. Consider two particles in contact as shown in figure 1.2. Superscripts denote the particle. **X** denotes the position vector of the particle and r its radius. ξ is the overlap and **n** is the unit vector from particle j to particle i.

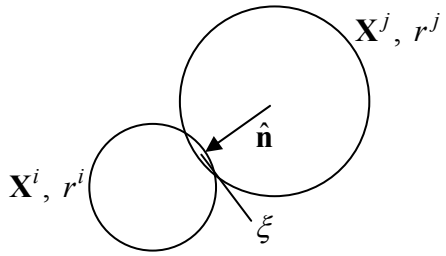

Figure 1.2. A schematic of two particles in contact

The total force acting on particle i from particle j is the sum of the forces along the normal direction due to the indentation ξ and along the tangent to the contact surface (perpendicular to **n**) due to friction. The friction also induces moments about the center of the particle i. The simplest description of the normal contact force is by defining the contact stiffness as a linear spring. However, for this research we use a Non-Linear Elastic Hertz contact law, where the contact force is proportional to $\xi^{3/2}$. The contact is modeled to include a viscous dissipative force opposing the relative normal motion of the particles. This force is proportional to the stiffness of the contact, relative normal velocities at the contact and the square root of the depth of indentation, ξ, ([14]), and is, thus, comparable to the elastic forces. The purpose of this viscous force is to filter out the high frequency vibrations associated with the elastic contact. Thus,

$$\mathbf{F}^{ij}_{Hertz} = \frac{4}{3}\frac{E}{\left(1-\nu^2\right)}\sqrt{\frac{r^i r^j}{r^i + r^j}}\xi^{3/2}\mathbf{n} \tag{1.1}$$

Where E is the elastic modulus of the material of the particle and ν is the Poisson's ratio. The contact damping force is given by

$$\mathbf{F}^{ij}_{Damping} = \alpha\frac{4}{3}\frac{E}{\left(1-\nu^2\right)}\sqrt{\frac{r^i r^j}{r^i + r^j}}\xi^{1/2}\left(-\dot{\xi}\right)\mathbf{n} \tag{1.2}$$

where α is the contact damping coefficient whose value can be prescribed based on the desired coefficient restitution for the impact of the two particles. The damping force acts such that it opposes the relative motion of the particles. The slip, tangential to the contact normal, is caused by both the relative translational sliding in that direction and the rotational velocities of the particles given by

$$\mathbf{v}^{ij}_{slip} = \left(\left(\mathbf{v}^i - \mathbf{v}^j\right) - \left(\mathbf{v}^i - \mathbf{v}^j\right)\cdot\mathbf{n}\right) + \left(\boldsymbol{\omega}^i r^i - \boldsymbol{\omega}^j r^j\right)$$

where $\mathbf{v}$ denotes the velocity of a particle and $\boldsymbol{\omega}$ is the angular velocity of a particle. Tangential forces act at the point of contact due to friction opposite to the net tangential slip. We use a viscous regularization of Coulomb's friction given by

$$\mathbf{F}^{ij}_{Friction} = -\mu\left|\mathbf{F}^{ij}_{Hertz}\right|\left(\frac{\left|\mathbf{v}^{ij}_{slip}\right|}{v_R}\right)^{1/m}\hat{\mathbf{v}}^{ij}_{slip} \tag{1.3}$$

Where μ is the coefficient of friction, v_R is the characteristic relative velocity of the particles under deformation (discussed in detail in chapter 2) and m is a large number. The moment induced by the friction on the particle is given by

$$\mathbf{M}^{ij} = \mathbf{r}^{ij} \times \mathbf{F}^{ij}_{Friction} \tag{1.4}$$

where r^{ij} is the vector from the center of particle i to the point of contact with particle j. Thus, the total force acting on particle i due to all its contacts is given by

$$\mathbf{F}^i = \sum_{j=1}^{contacts} \mathbf{F}^{ij}_{Hertz} + \mathbf{F}^{ij}_{Damping} + \mathbf{F}^{ij}_{Friction} \tag{1.5}$$

with a similar summation for computing the net moments. Once the net force acting on a particle is computed, its position can be integrated in time. A simple Verlet scheme is followed for the time integration given by

$$\mathbf{X}^i\left(t+\delta t\right) = 2\mathbf{X}^i\left(t\right) - \mathbf{X}^i\left(t-\delta t\right) + \left(\frac{\mathbf{F}^i}{m^i}\right)\left(\delta t\right)^2 \tag{1.6}$$

where δt is the time increment and m^i is the mass of particle i. This method has an error of $O(\delta t^4)$ for the positions and an error of $O(\delta t^2)$ for the velocities.

Having outlined the numerical method, we focus on defining the specific problems that will be addressed in this work. While the DEM is a convenient way to describe particle motion and observe the micromechanics, it is computationally intensive due to the vast difference between the integration timescale and the observation timescale i.e. the time increment δt is much smaller than the timescale of the computational experiments. To increase the magnitude of the time increment, the mass density of the particles is assumed to be many orders of magnitude higher than reality [15, 16]. This approach, however, induces inertial effects into the simulation, subject to the deformation parameters prescribed. In chapter 2, this problem is addressed by deriving a macroscopic quasistatic coefficient which ensures low inertial effects. Further, a two timescales algorithm is presented to improve computational efficiency.

As mentioned earlier, the strain localizations in granular materials are caused due to local instabilities of the supporting force chain network. While investigations have identified the stages in the formation of these instabilities [4], the most important which cause these instabilities – boundary conditions have not been explored, primarily due to lack of alternatives to the standard biaxial and triaxial setups to impose deformation. We develop minimal boundary conditions which impose only the strain and not the rigidity associated with standard boundary conditions in chapter 3. The effect of the boundary conditions on the micromechanics of the granular assembly is explored. Another interesting quality granular materials display is the high rotation of particles in the strain localization zone, also known as shear bands. Granular materials display a typical length scale through which these high rotations propagate. This issue has not been resolved. We address this length scale of rotations with respect to the strength of force chains in chapter 4 and it is shown that the width of a shear band is closely related to this rotation length scale.

References

1. Drescher A & DeJosselin DeJong G. Photoelastic verification of a mechanical model for the flow of a granular material. Journal of the Mechanics and Physics of Solids 1972; 20: 337-351.
2. Kuhn, M.R., 1999. Structured deformation in granular materials. Mechanics of materials. 31, 407 – 429.
3. Radjai F, Jean M, Moreau J-J, Roux S. Force distribution in dense two-dimensional granular systems. Physical Review Letters 1996; 77(2), pp. 274-277.
4. Tordesillas A, Force chain buckling, unjamming transitions and shear banding in dense granular assemblies. Philosophical Magazine. v 87, n 32, 4987–5016.
5. Fazekas, S., Torok, J. & Kertesz, J. 2007 Critical packing in granular shear bands. Phys. Rev. E 75, 011302.
6. Cundall, P.A., Strack, O.D.L., 1979, A discrete numerical model for granular assemblies. Geotechnique. 29, 47-65.
7. Thornton C, Barnes D.J, 1986, Acta Mechanica, 64, 45-61.
8. Bardet JP & Proubet J. A numerical investigation of the structure of persistent shear bands in granular media, Geotechnique 1991; 41(4), pp. 599-613.
9. Iwashita K. & Oda M. Micro-deformation mechanism of shear banding process based on modified distinct element method. Powder Technology 2000; 109: 192-205.
10. Masson S, Martinez J, 2001, Journal of Engineering Mechanics, v127, n10, 1007-1016.
11. Hu N, Molinari J.F, 2004, Journal of the Mechanics and Physics of Solids, 52, 499-531
12. Fazekas S, Torok J, Kertesz J, Wolf DE. Morphologies of three-dimensional shear bands in granular media, Physical review E 2006; 74(3), pp. 031303-1 – 031303-6.

13. Oda M & Kazama H. Microstructure of shear bands and its relation to the mechanisms of dilatancy and failure of dense granular soils. Geotechnique 1998; 48(4), pp. 465-481.

14. Brilliantov NV, Spahn F, Hertzsch JM and Poschel T. Model for collisions in granular gases. Physical Review E 1996; 53 (5), pp. 5382 – 5392.

15. Martin CL, Bouvard D, Shima S. Study of particle rearrangement during powder compaction by the Discrete Element Method, Journal of the Mechanics and Physics of Solids 2003; 51: 667 – 693.

16. Thornton C & Antony SJ. Quasi-static shear deformation of a soft particle system, Powder Technology 2000; 109: 179–191.

International Journal for Numerical Methods in Engineering (Under review)

2. Acceleration of DEM algorithm for quasistatic processes

Jagan M. Padbidri & Sinisa Dj. Mesarovic*

School of Mechanical and Materials Engineering, Washington State University, Pullman, WA

*mesarovic@mme.wsu.edu

2.1 Introduction

The innovative experimental methods [1-5] have yielded significant insight into deformation mechanisms of granular matter. Nevertheless, the detailed study of particle motion requires numerical simulation. The numerical method used in such simulations is known as the discrete element method (DEM). It is essentially a particle dynamics method similar to molecular dynamics, but with the short range (contact) forces, and the additional degrees of freedom – rotations. The main computational problem of DEM is the vast difference between the time scale of numerical integration and observation time scale. This requirement for small integration time steps results in a practical problem similar to the one faced by practitioners of molecular dynamics – many realistic experiments cannot be simulated economically. The problem arises from high natural frequencies associated with the system: high contact stiffness and low mass of the particles. This is particularly ill-suited for simulations of macroscopically quasi-static static deformation, associated with numerous problems in geomechanics. The mechanism of quasistatic deformation is such that at any time most particles are in (or near) local stable equilibrium. The remaining few particles are accelerating rapidly following local configurational instability. Any particular particle spends most of its life in slow (near

equilibrium) relative motion with respect to its neighbors, with only short bursts of accelerated motion. The relevant experimental time scales are in seconds, while the integration time step, required to resolve particle dynamics, is of the order of 10^{-10} seconds. Implicit computational schemes have been developed [6], but these do not parallelize well, so that particle dynamics schemes appear to be the only promising direction.

Since the inception of the DEM [7], researchers have tried to circumvent the problem of time scale separation and accelerate the DEM computations. For macroscopically quasistatic processes, a commonly used method is to increase the mass of the particles by a few orders of magnitude [8-10] which eliminates the high frequency oscillations of the particle. Two questions immediately arise in connection with such methods:

(1) When is a process macroscopically quasistatic?

(2) How does such change in dynamics of individual particle affect the macroscopically quasistatic deformation process?

We will address these questions here. The questions are also relevant for algorithms which use adaptive damping mechanisms [11]. In such formulations, numerical stability is achieved by using both: mass scaling and variable coefficients of damping, thus allowing a larger time step and fewer calculations during DEM simulations. This approach implicitly contains the assumption that the process is macroscopically quasistatic. Otherwise, the changes in dynamics of an individual particle are bound to change the overall dynamics.

The aforementioned computational inefficiencies affect the rotational degrees of freedom to a greater extent i.e. the time step required for the integration of rotations is smaller than that for translations. Using a very small time step for all degrees of freedom guarantees accuracy but retains the computational handicap. In this paper, we quantify the difference of timescales

between the degrees of freedom and propose a two-timescales algorithm. The algorithm is based on the concept of inertial manifolds [12] which distinguishes between *fast* and *slow* variables, rotations and translations respectively, and serves to increase the computational efficiency.

The work is organized as follows. In Section 2.2, we present the scaled governing differential equations and the conditions for quasistatic deformation. The scaling of the force equations and the issue of determining a time step is addressed in Section 2.3. The motivation for separation of time scales is presented in Section 2.4 followed by the proposed two-timescales algorithm. The computational setup is discussed in Section 2.5 and the results are presented in Section 2.6.

2.2 Global scaling of governing equations and quasistatic deformation

Consider an assembly of N particles. Particle k is characterized by its radius R^k, and mass m^k. The equations of motion for positions $\mathbf{x}^k$, velocities $\mathbf{v}^k$, and angular velocities $\boldsymbol{\omega}^k$, are:

$$\begin{aligned} m^k \dot{\mathbf{v}}^k &= \sum\nolimits_j \mathbf{f}^{kj} \qquad \left(= \mathbf{F}^k\right), \\ \dot{\mathbf{x}}^k &= \mathbf{v}^k, \qquad\qquad\qquad\qquad k = 1,\ldots,N. \\ \tfrac{1}{2}\left(R^k\right)^2 m^k \dot{\boldsymbol{\omega}}^k &= \sum\nolimits_j \mathbf{r}^{kj} \times \mathbf{f}^{kj} \quad \left(= \mathbf{M}^k\right), \end{aligned} \tag{2.1}$$

$\mathbf{r}^{kj}$ is the position vector of the contact point of particle k with particle j, measured from the center of k. Vectors and tensors are denoted using boldface. The definition of interaction forces $\mathbf{f}^{kj}$ is given in Appendix A, and their scaling is discussed in Section 2.3. For now, we only consider the characteristic magnitudes of forces and moments, and concentrate on the equations of motion. Let the average particle radius be R and the average mass is m. The volume is L^3, so that $L = 2RN^{1/3}$. The densely-packed assembly is subjected to pressure p, and imposed strain

rate $\dot{\varepsilon}_0$. The magnitude of inter-particle forces in equilibrium, f_0, is characterized by the pressure, which implies the characteristic indentation depth d_0:

$$f_0 = pL^2/N^{2/3}, \text{ and } d_0 = \left(f_0/K\right)^{2/3}, \tag{2.2}$$

where $K = 4\bar{E}R^{1/2}/3\sqrt{2}$ is the Hertz contact coefficient, with $\bar{E} = E/2(1-\nu^2)$ being the effective plane-strain elastic modulus.

With the imposed nominal strain rate $\dot{\varepsilon}_0$, there are two characteristic velocities: the externally imposed one v_0, and the relative velocity of neighboring particles v_R:

$$v_0 = \dot{\varepsilon}_0 L/2, \text{ and } v_R = 2\dot{\varepsilon}_0 R. \tag{2.3}$$

It is the relative velocity that determines the order of magnitude of angular velocities:

$$\omega_0 = v_R/2R = \dot{\varepsilon}_0. \tag{2.4}$$

The externally imposed time scale is:

$$t_0 = 1/\dot{\varepsilon}_0. \tag{2.5}$$

The position **x** will be scaled with $L/2$. Denote non-dimensional quantities with overbars, and the derivatives with respect to the non-dimensional time with prime. For simplicity, we drop the particle indices and order-one constants such as the ratio of particle mass m^k and the average particle mass m. The resulting typical non-dimensional equations are:

$$\begin{aligned} \frac{mv_0}{f_0 t_0}\bar{\mathbf{v}}' &= \bar{\mathbf{F}}, \\ \bar{\mathbf{x}}' &= \bar{\mathbf{v}}, \\ \frac{2R}{L}\frac{mv_0}{f_0 t_0}\bar{\boldsymbol{\omega}}' &= \bar{\mathbf{M}}. \end{aligned} \tag{2.6}$$

We consider macroscopically non-inertial (quasistatic) processes, which are characterized by the small ratio of the nominal inertial force and the nominal pressure force. For the system to

be macroscopically non-inertial (quasistatic), the equations of motion must reduce to equilibrium equations in the global (average) sense. Let $\boldsymbol{\sigma}$ be the stress tensor, ρ the mass density of the assembly, and **v** the velocity field. The quasistatic condition for the volume $V = L^3$ can be written as

$$\int_V |\nabla \cdot \boldsymbol{\sigma}| dV \gg \int_V \rho \left| \frac{d\mathbf{v}}{dt} \right| dV. \tag{2.7}$$

Let the pressure *p* represent the magnitude of stresses. If gradients of stress components are of the order p/L, the l.h.s. of (2.7) has magnitude pL^2. On the r.h.s., the mass density is assumed to be uniform and can be expressed in terms of the average particle mass *m*, number of particles *N*, and the volume L^3:

$$\rho = Nm/L^3 \tag{2.8}$$

Let the position vector **x** be measured from the geometric center of the volume. Assume the affine velocity field with characteristic velocity gradient $\mathbf{G}_0$. Then:

$$\mathbf{v} = \mathbf{G}_0 \cdot \mathbf{x} \Rightarrow d\mathbf{v}/dt = \mathbf{G}_0 \cdot \mathbf{v} = \mathbf{G}_0 \cdot \mathbf{G}_0 \cdot \mathbf{x} \tag{2.9}$$

Take $[\mathbf{G}_0]_{ij} = \dot{\varepsilon}_0 \delta_{2i} \delta_{2j}$, then:

$$\int_V \rho \left| \frac{d\mathbf{v}}{dt} \right| dV \approx \frac{Nm}{L^3} \dot{\varepsilon}_0^2 \frac{L^4}{2} = Nm\dot{\varepsilon}_0^2 \frac{L}{2}. \tag{2.10}$$

The condition (2.7) can then be written as

$$pL^2 \gg Nm\dot{\varepsilon}_0^2 \frac{L}{2} = N \frac{mv_0}{t_0}, \text{ or,} \tag{2.11}$$

$$\phi = \frac{Nmv_0}{pL^2 t_0} \ll 1. \tag{2.12}$$

The *quasistatic coefficient,* ϕ, is derived from the condition that the deformation process is macroscopically quasistatic (2.7), i.e., that the macroscopic governing equations are well approximated by equilibrium equations for a continuum. Using (2.2 - 2.5), it can also be written as:

$$\phi = \frac{mv_0}{f_0 t_0} N^{1/3} = \frac{m\dot{\varepsilon}_0^2}{4pR} N^{2/3} \ll 1. \tag{2.13}$$

The quasistatic coefficient must be small to ensure the macroscopically quasistatic nature of the deformation process. The last expression for ϕ in (2.13) is particularly instructive. For a given pressure, deformation rate, particle size and number of particles, it provides a criterion for application of the commonly used large mass method for accelerating the time integration. Roughly, if the quasistatic coefficient is small, and it remains small after increasing the particle mass, we expect that the resulting changes in micro-scale dynamics will not affect the macroscopically quasi-static nature of the problem. In contrast to the *inertia number* in [13], we conclude that the *quasistatic coefficient* (2.13) must depend on the size of the assembly. For a prescribed strain rate, the characteristic velocity of a particle (and hence – its kinetic energy), must depend on the size of the assembly.

The large number of particles can be represented by a non-dimensional coefficient:

$$\psi = 2R/L = N^{-1/3} \ll 1. \tag{2.14}$$

Using (2.13) and (2.14), the governing equations (2.6), can be rewritten as:

$$\begin{aligned} \phi\psi\,\bar{\mathbf{v}}' &= \bar{\mathbf{F}}\left(\bar{\mathbf{x}}, \bar{\mathbf{v}}, \bar{\boldsymbol{\omega}}\right), \\ \bar{\mathbf{x}}' &= \bar{\mathbf{v}}, \\ \phi\psi^2\,\bar{\boldsymbol{\omega}}' &= \bar{\mathbf{M}}\left(\bar{\mathbf{x}}, \bar{\mathbf{v}}, \bar{\boldsymbol{\omega}}\right). \end{aligned} \tag{2.15}$$

The coefficients for the equations in (2.15) contain the term $\psi = N^{-1/3}$. This is to be expected since the position, and correspondingly the velocity, of a particle has been scaled with respect to the sample size. The small parameter in the 1st equation, $\phi\psi$, reflects physical nature of the deformation process, whereby slow, near-affine motion of particles is interrupted by intermittent bursts of high acceleration following locally instabilities. The small parameter in the 3rd equation, $\phi\psi^2$, is the result of the physical nature of rotations, which are driven by *relative* translations. The additional factor ψ in the 3rd equation of (2.15) implies that the characteristic relaxation time for rotations is much shorter than that of translations, i.e., the rotations are *fast* variables, while the translations are *slow* variables.

2.3 Scaling and relaxation time of contact forces

The time step for simulations is usually determined by the requirement to accurately represent the variations of contact forces with time [7, 8, 14]. The impact between two free-flying elastic particles may be characterized by a range of values of the coefficients of restitution. However, in a densely packed assembly, each particle is subjected to a number of frictional contacts, so that most of its kinetic energy is dissipated in impacts with its neighbors, resulting in a very low effective coefficient of restitution. Brilliantov et al [15] proposed a nonlinear viscoelastic impact law, with stiffness-proportional contact damping, such that, at high impact velocities, most of the kinetic energy of impact is dissipated, while in slow contact, most of the work is stored as elastic energy.

The relative normal (indentation) velocity between particles *k* and *j*, denoted d^{kj}, and the corresponding normal force f_n^{kj}, positive in compression, are discussed in detail in Appendix A. The resulting normal contact law is

$$f_n^{kj} = K^{kj}\left(d^{kj}\right)^{3/2} + TK^{kj}\left(d^{kj}\right)^{1/2}\dot{d}^{kj}. \tag{2.16}$$

where *T* is the contact damping coefficient. The forces vary on a time scale much shorter than the macroscopic time scale t_0 (2.5). Normalized with f_0 (2.2), and the time t_0, the equation (2.16) reads

$$\overline{f}_n = \overline{d}^{3/2} + \left(\frac{T}{t_0}\right)\overline{d}^{1/2}\overline{d}'. \tag{2.17}$$

To accurately integrate the governing equations (2.1), the characteristic relaxation time of the contact forces, arising from (2.16, 2.17) must be numerically resolved. To estimate the relaxation time, we consider the impact problem of two particles with no initial indentation and initial velocity equal to the characteristic relative velocity, v_R (2.3). Both, the coefficient of restitution (ratio of the relative velocities of the disks after and before impact) and the characteristic relaxation time, are 1-1 functions of the parameter T. Thus, we can represent the relaxation time as function of the coefficient of restitution (Figure 2.1).

The magnitude of the tangential force is modeled as viscous regularization of the Coulomb law with the characteristic velocity v_R (2.3). The relative sliding velocity between the particles s^{kj}, and the corresponding tangential force f_t^{kj}, are defined in Appendix A:

$$f_t^{kj} = \mu f_n^{kj}\left(\frac{s^{kj}}{v_R}\right)^{1/c}, \tag{2.18}$$

where μ is the coefficient of friction and c is a large number. With forces scaled by f_0 and $\overline{s} = s/v_R$, the non-dimensional form of (2.18) is

$$\overline{f}_t = \mu \overline{f}_n \overline{s}^{1/c}. \tag{2.19}$$

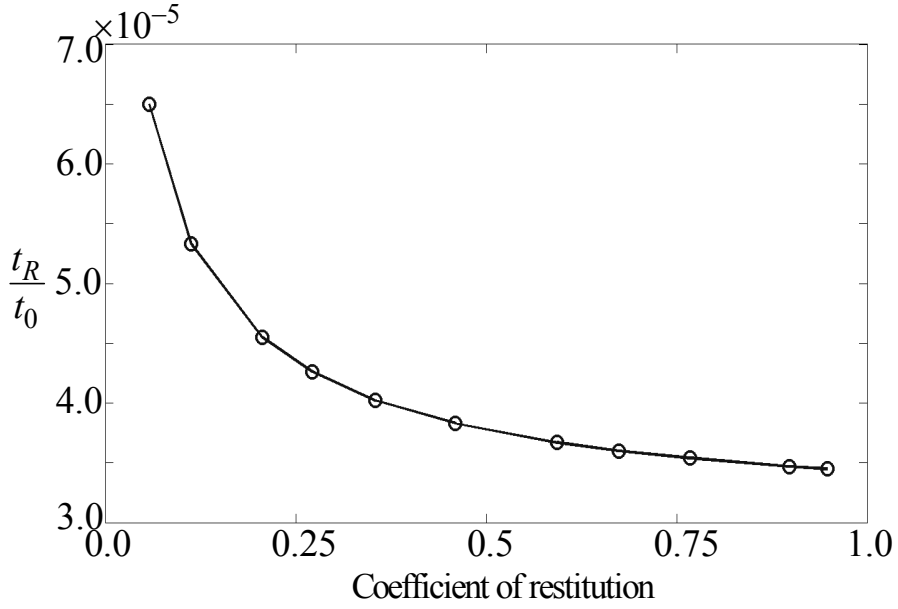

Figure 2.1. The relaxation time as a function of the coefficient of restitution, arising from governing equation (16, 17).

2.4 The two-timescales algorithm

The inertial manifold method, proposed by Gear and Kevrekidis [12] is based on the existence of slow and fast variables, such that the fast variables are driven by the evolution of slow variables and quickly converge to the inertial manifold governed by the slow variables. The method is applicable to stiff systems such as the one defined by DEM governing equations (2.1, 2.15).

In this case the fast variables are the rotations (2.15). Using a very small time step, corresponding to the 3rd equation of (2.15) yields accurate time integration. However, this approach is computationally inefficient. The general idea is to first take a large time step with

slow variables, thus approximating the inertial manifold. Then few small time steps with fast variables are taken, presumably sufficient for fast variables to converge to the manifold.

In the large time step, slow variables can be integrated independently, if the effect of fast variables on the evolution of slow ones is weak. We have found that that is not the case for the DEM equations. Moreover, the major expense in computational time is the computation of forces. Once forces are computed, the computation of moments and time integration of rotations are relatively inexpensive. Conversely, in the short time steps, one could integrate only fast variables, i.e., rotations. However, to compute moments, one must compute forces, and with forces computed, integration of slow variables (translation) is expedient.

We have tested several integration schemes involving the large time step, Δt, and the small time step [cf. (2.15)]:

$$\delta t = \Delta t / N_S ; \quad N_S \approx 1/\psi . \tag{2.20}$$

The following should be noted:

- Interpolating the slow variables within the large time step (to perform integration with small time steps, yields practically no benefit. The forces still must be computed in each small time step.
- Interpolating forces is not reasonable; they vary strongly with fast variables, thus rendering any force interpolation inaccurate.

The only integration scheme that yielded measurable benefits (albeit moderate) includes integration of all variables through a series of large and small time steps. At the end of the large time step, the fast variables are inaccurate, but then rapidly converge towards the manifold. The procedure is as follows.

(1) Take a large time step of size $n\delta t, n < N_S$.

(2) Take q successive steps with the small time step δt.

(3) Repeat steps (1) and (2) m times so that $m(n+q) = N_S$.

2.5 Problem setup

We consider the two-dimensional problem shown in Figure 2.2. The initial packing is achieved using the algorithm proposed by Jodrey and Tory [16] in which the path of each particle is followed, as it settles, driven by gravity, from a suspension into a randomly packed bed. The particle radii are random, uniformly distributed on the interval $[0.5,\ 1]$. The pressure is applied directly, on the boundary, using the method described below. After ramping the pressure, the top and bottom rigid plates are moved with the constant velocity according to the prescribed strain rate.

To impose the pressure (or, in general, traction) boundary conditions, a definition of the granular continuum is needed. We use Bagi [17] and Satake [18] formulation of a continuum based on graph theory. The complementary graph to the one obtained by Dirichlet tessellation is the Delaunay graph. Its cells are simplexes (triangles in 2D and tetrahedra in 3D), the nodes are centers of particles, and edges connect nearest neighbors.

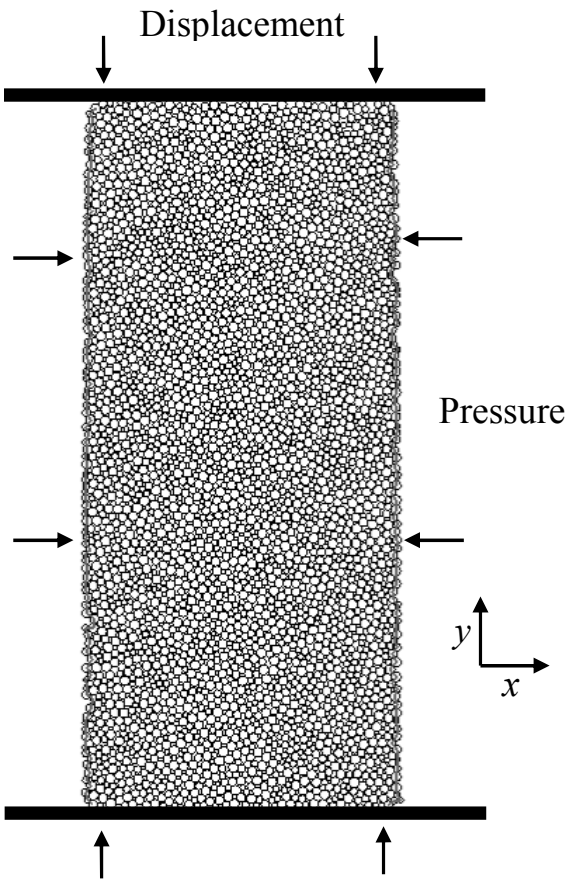

Figure 2.2. Schematic of a granular assembly with pressure imposed directly on the boundary particles. The gray lines indicate the lateral boundaries on which the pressure is applied.

Consider a Delaunay tetrahedron. The 12 degrees of freedom corresponding to nodal velocities are represented *exactly* by: one velocity vector (rigid body translation), one skew symmetric tensor (rigid body rotation), and, one symmetric tensor (strain rate). This defines the kinematics of a C^0 continuum (piecewise constant strain rate). Moreover, the Cauchy stress for granular materials, as defined by Christoffersen et al [19], is the work conjugate of this strain rate, so that the granular assembly is equivalent to the mesh of constant strain finite elements. Both traction and kinematic boundary conditions can be applied accordingly [20, 21]. More detailed application of kinematic boundary conditions is presented in the forthcoming paper [22].

This approach requires that the boundary of the Delaunay graph be defined, which has small computational cost associated with it. The boundary is updated throughout the simulation process after every 250 time steps.

The definitions for ϕ (2.13) and ψ (2.14) for the 2D case and the parameters used for the simulations are described in Appendix B. For the parameters used, the quasistatic coefficient is found to be of the order 10^{-4} (with increased mass included). The relevant time step for the simulations can be deduced from Figure 2.1; the relaxation time for the impact problem is $O\left(10^{-5}t_0\right)$. To numerically resolve the relaxation time interval, he appropriate time step for the translations would be $\Delta t \approx O\left(10^{-6}t_0\right)$. However, granular materials typically show intermittent bursts of high velocity. To be on the safe side, we choose the time step of $\Delta t = 0.5\times10^{-7}t_0$ for translations. The rotations are about 50 times faster than translations (Appendix B), so that $\delta t = 10^{-9}t_0$. Three time stepping algorithms are used for the same initial sample and boundary conditions:

I. One timescale DEM with time step $\Delta t = 0.5\times10^{-7}t_0$.

II. Two-timescales DEM with time step $\Delta t = 0.5\times10^{-7}t_0$ and 50 substeps with different combinations of *n, q* and *m* (Section 3) represented as II: *m*(*n* + *q*).

III. One timescale DEM with time step $\delta t = 10^{-9}t_0$ (Benchmark case).

2.6 Results and discussion

The generated sample of 2D granular material is over-consolidated, i.e., below the critical line [23]. Therefore, we expect to see dilatancy of the sample. This is an important qualitative criterion for the accuracy of computations. The components of strain tensor are computed using the Bagi-Satake definitions [17, 18] discussed in the previous section. We consider two samples of different size (983 and 3970 particles) to observe possible size effects.

The evolution of volumetric strain with the imposed axial strain is shown in Figure 2.3. Dilatancy is observed for the cases II and III, where smaller time steps are used. In both cases, the volumetric strain reaches a peak value and then drops down as a dominant shear band emerges. For all combinations (*m, n, q*), the new algorithm (II) agrees well with the benchmark (III), until the critical state is reached. Once the critical state is achieved, the new algorithm becomes sensitive to the combination of parameters (*m, n, q*). The case 5(5+5) appears to be the best choice. When only the large time step (I) is used, no dilation is observed. However, the volumetric strain does reach a steady state at about 9% axial strain. The size effects are noticeable; the maximum dilation of the small sample is about twice the one of the large sample.

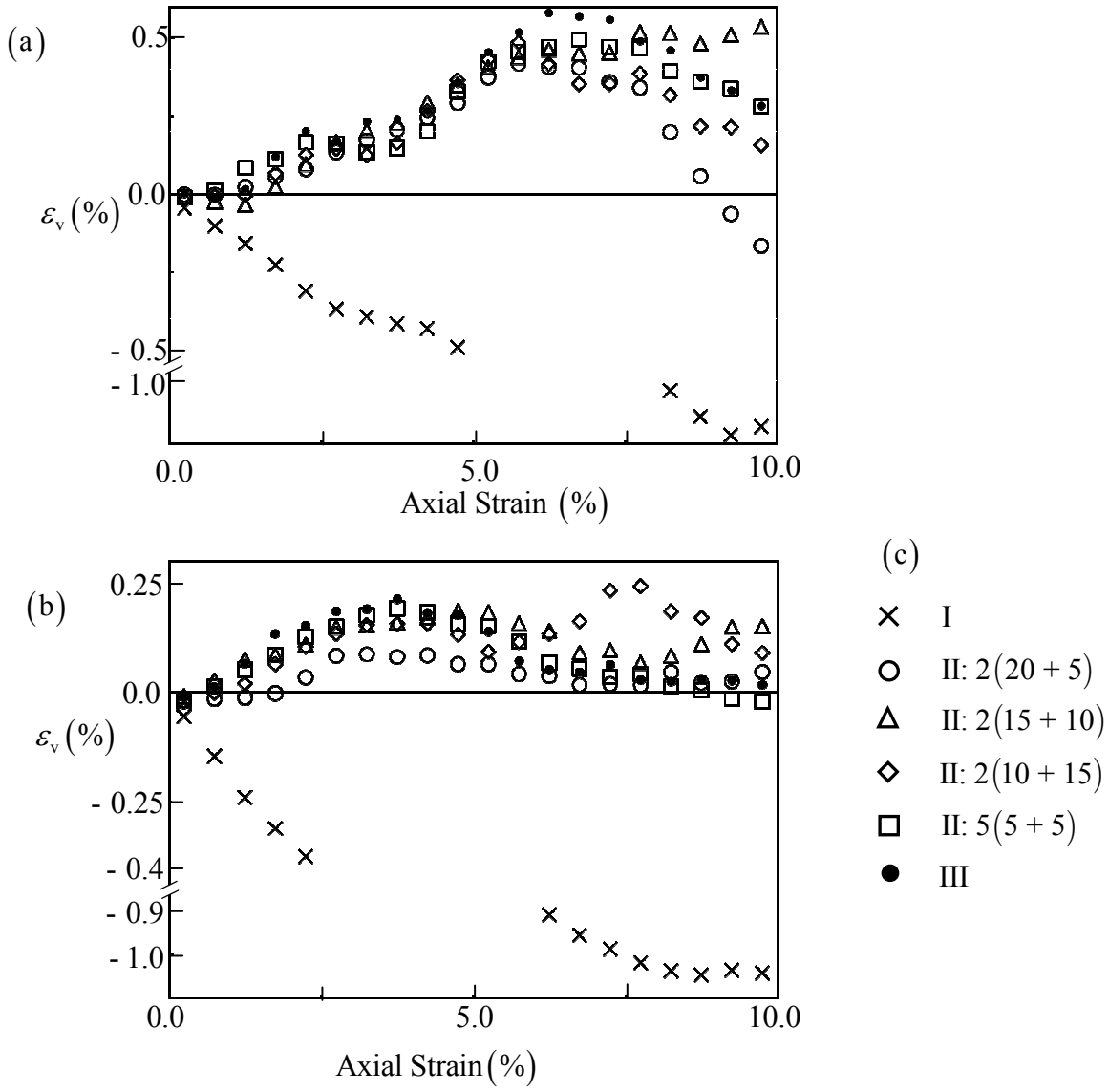

Figure 2.3. Volumetric strain evolution for: (a) 983 disk assembly, (b) 3970 disk assembly. (c) Legend.

The assembly average of relative (absolute) slip rate between particles is plotted in Figure 2.4, as function of axial strain. For a larger time step (I), the average slip velocity increases with the size of the assembly (Figures 2.4a, b), though their magnitude at the beginning of the deformation process is roughly the same ($\approx 3v_R$). This is the result of increasing time-scale difference between rotations and translations with the size of the assembly [cf. (2.14, 2.15)]. The new algorithm (II) follows the benchmark case closely for all combinations (*m, n, q*), particularly

for the larger assembly. The slip velocities are measured at the end of the sequence of q small time steps, so that the measured velocities have converged to the manifold.

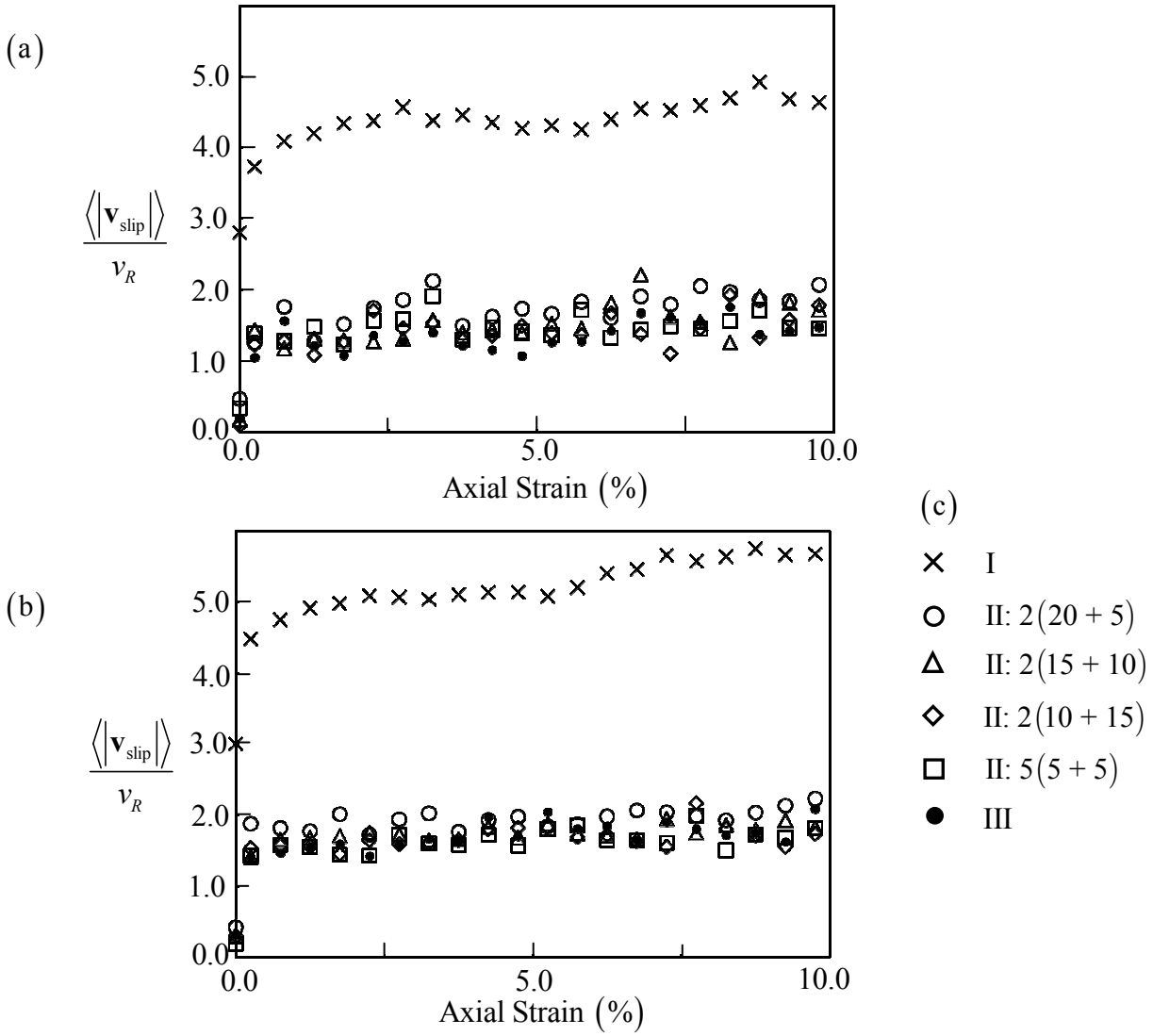

Figure 2.4. Normalized assembly average of absolute slip velocity at contacts for: (a) 983 disk assembly, (b) 3970 disk assembly. (c) Legend.

The evolution of stress ratios is shown in Figure 2.5. The differences are smaller here. Nevertheless the large step algorithm (I) is distinctly softer; inaccurate integration effectively makes slip easier and favors it over rotation, as the basic mechanism for tangential interparticle motion.

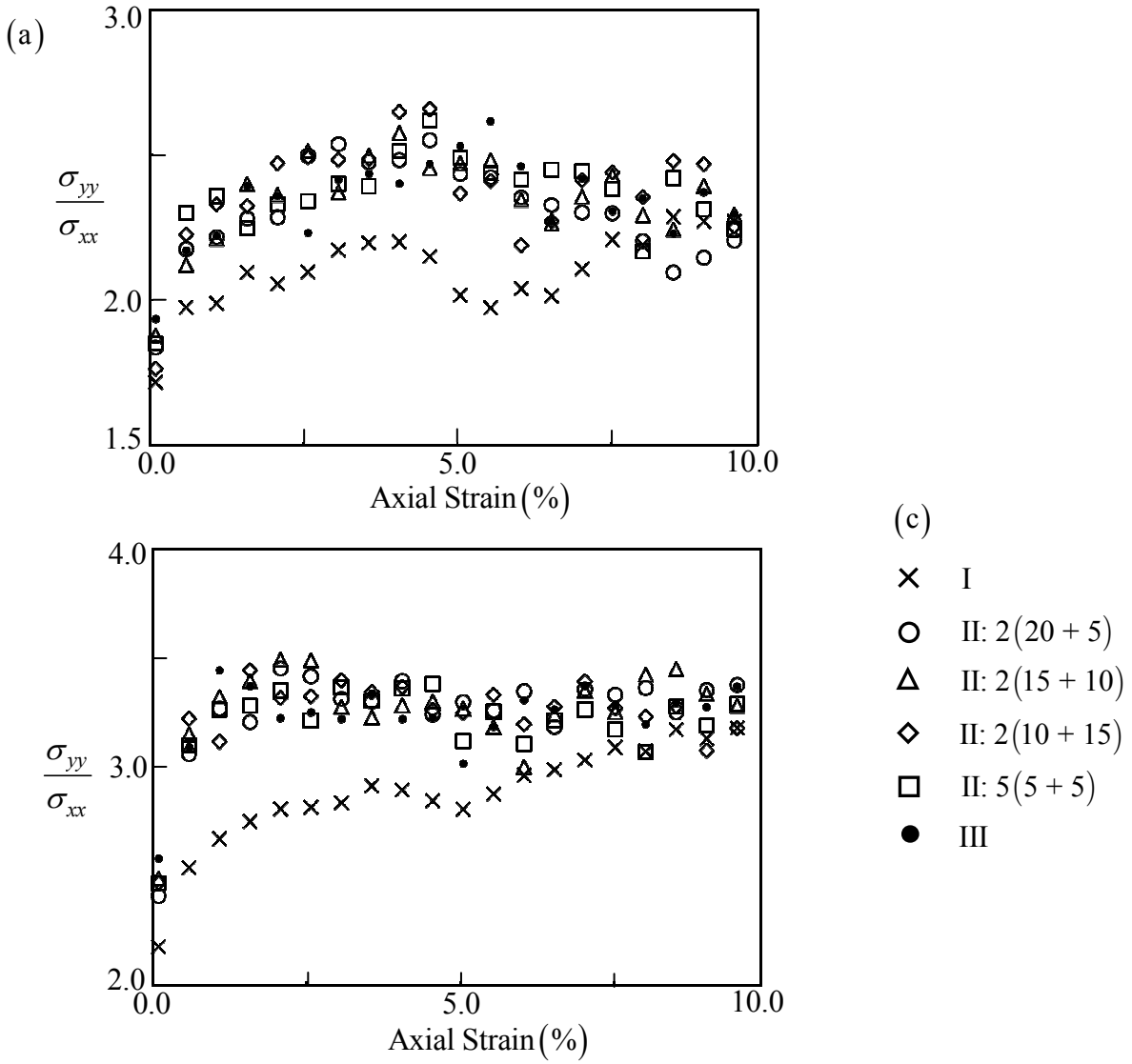

Figure 2.5. Stress ratio evolution for: (a) 983 disk assembly, (b) 3970 disk assembly. (c) Legend. The stress $\sigma_{xx} = p$ is the fixed lateral pressure. Initially $\sigma_{yy}/\sigma_{xx} = 1$.

Finally, we consider the accuracy of the flow pattern in the assembly. A convenient representation is the one of displacement vectors relative to the uniform strain field, corresponding to the affine displacement field [cf. (2.9)]. Such plots of spatial fluctuations of displacements are shown in Figures 2.6 and 2.7 for the two assemblies. The agreement between

the patterns produced by the new algorithm, II: 5(5+5), and the benchmark (III) is apparent. The large step runs (I) produce a very different pattern. Other runs in the II: $m(n+q)$, produce patterns that increasingly deviate from the benchmark, with increasing n. The disagreement becomes more pronounced when the critical state is reached.

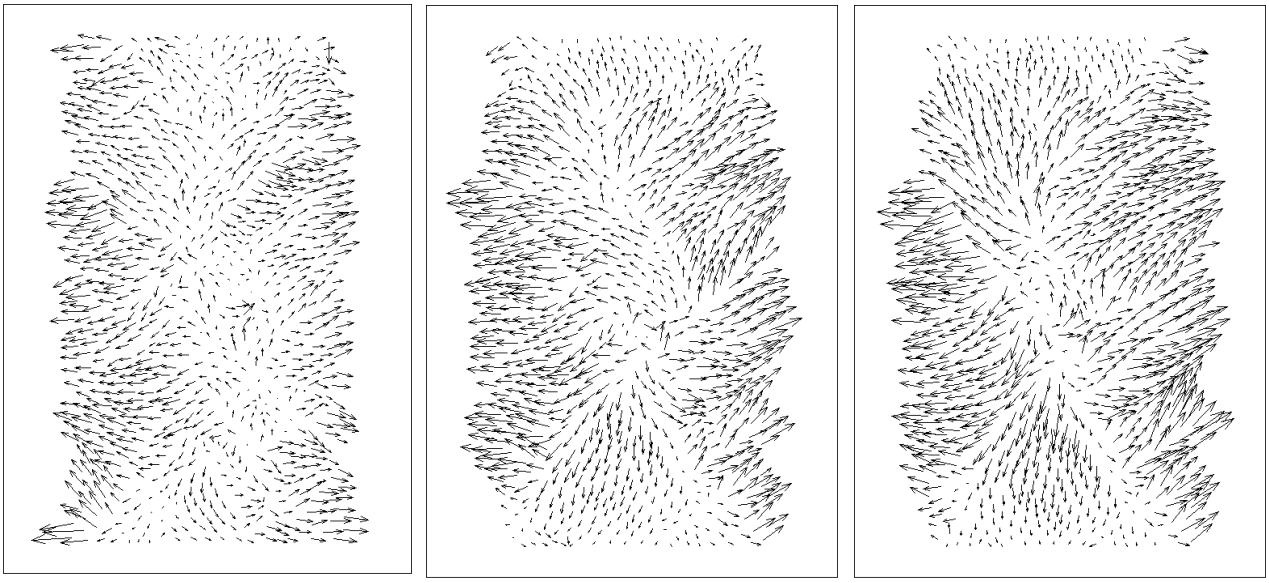

(a) (b) (c)

Figure 2.6. Displacement vectors relative to the affine displacement with uniform ε_{yy} for the 983 particle assembly, for the macroscopic axial strain interval: 5% to 10%. (a) Large step – I, (b) Two-timesteps – II: 5(5 + 5), (c) Benchmark – III.

In Table 2.1, we list the computational accelerations relative to the benchmark case for different combinations (*m, n, q*). Theoretical acceleration is easily computed as $(n+q)/(1+q)$. Clearly, the two-timesteps algorithm, provides a moderate improvement in computing time. The computational acceleration is better if one considers only cases below critical state, where more favorable combinations (*m, n, q*) can be used. Once the critical state is reached, the system

becomes much more sensitive to the time-stepping algorithm, and only the algorithm II: 5(5 + 5) remains viable.

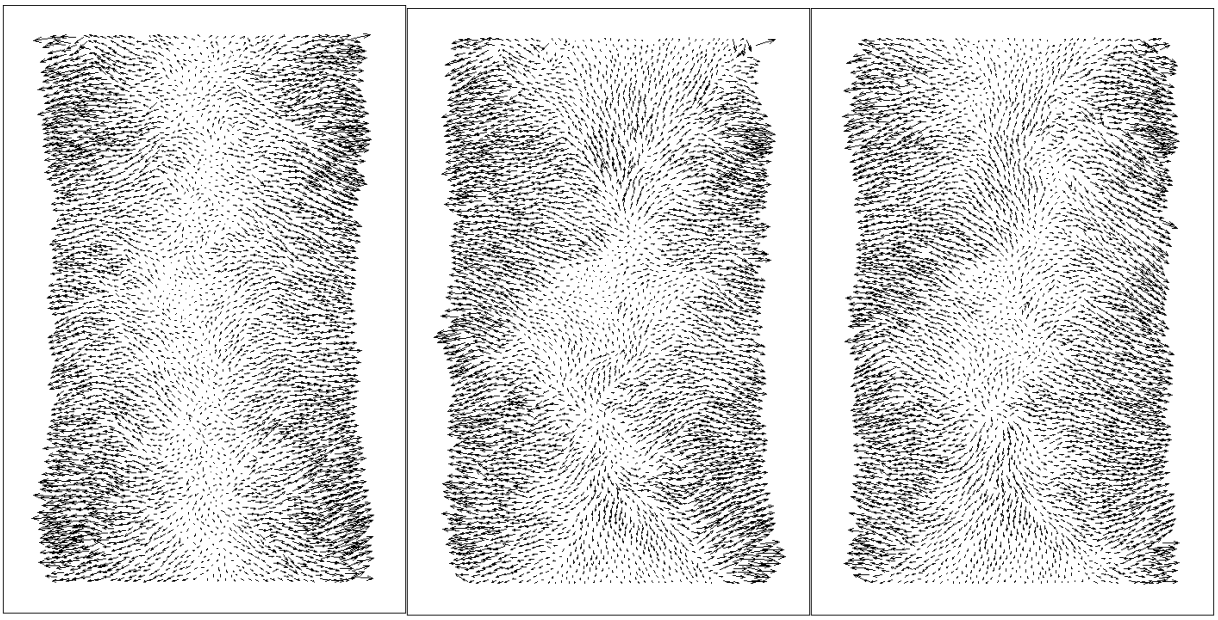

(a) (b) (c)

Figure 2.7. Displacement vectors relative to the affine displacement with uniform ε_{yy} for the 3970 particle assembly, for the macroscopic axial strain interval: 5% to 10%. (a) Large step – I, (b) Two-timesteps – II: 5(5 + 5), (c) Benchmark – III.

Table 2.1: Computational acceleration for the two-time-steps algorithm.

	983 Disks	3970 Disks	Theoretical
II: 2(20 + 5)	4.0305	4.0816	4.1667
II: 2(15 + 10)	2.2232	2.2272	2.2727
II: 2(10 + 15)	1.56	1.561	1.5625
II: 5(5 + 5)	**1.6573**	**1.6567**	**1.6667**
III	**1.0**	**1.0**	**1.0**

2.7 Conclusions

Based on the dimensional analysis of the DEM equations, we have derived the criterion for the macroscopically quasistatic process. This resulting quasistatic coefficient determines the validity of computational acceleration techniques, such as the increased mass method.

Dimensional analysis of the governing differential equations has yielded different characteristic timescales associated with translational and rotational degrees of freedom. Dimensional analysis of contact laws provided the force relaxation time, which determines integration time step.

The two-timescales algorithm, based on the concept of inertial manifold and taking advantage different timescales associated with translations and rotations, has been developed and tested for several combinations of short and long time steps. It provides modest computational acceleration, particularly at critical state. The new algorithm preserves the accuracy of computations.

Acknowledgements

This research was supported in part by US DOE/MICS, Grant # DE-FG02-05ER25709.

Appendix A

The total force on particle *k* at contact *kj* is:

$$\mathbf{f}^{kj} = f_n^{kj}\mathbf{n}^{kj} - f_t^{kj}\mathbf{t}^{kj}. \tag{2.A1}$$

With unit inward normal to particle *k* at contact *kj*, defined as $\mathbf{n}^{kj} = (\mathbf{x}^k - \mathbf{x}^j)\Big/\left|\mathbf{x}^k - \mathbf{x}^j\right|$, The contact indentation and its rate are

$$d^{kj} = \left\{\begin{array}{cc} R^k + R^j - \left|\mathbf{x}^k - \mathbf{x}^j\right|, & \text{if } d^{kj} > 0 \\ 0, & \text{otherwise} \end{array}\right\}, \tag{2.A2}$$

$$\dot{d}^{kj} = \left\{\begin{array}{cc} \left(\mathbf{v}^k - \mathbf{v}^j\right)\cdot\mathbf{n}^{kj} & \text{if } d^{kj} > 0 \\ 0 & \text{otherwise} \end{array}\right\}. \tag{2.A3}$$

The normal force, positive in compression, is defined as

$$f_n^{kj} = K^{kj}\left(d^{kj}\right)^{3/2} + TK^{kj}\left(d^{kj}\right)^{1/2}\dot{d}^{kj}, \tag{2.A4}$$

where *T* is the contact damping coefficient. To define tangential forces, we first define relative tangential velocities at the contact *kj*. Let the relative contact position, with respect to the center of particle *k*, be defined as

$$\mathbf{r}^{kj} = -R\mathbf{n}^{kj}, \tag{2.A5}$$

Using the tangential projection tensor, $\mathbf{P}^{kj} = \mathbf{I} - \mathbf{n}^{kj}\mathbf{n}^{kj}$, we write the tangential component of relative velocity as

$$\mathbf{s}^{kj} = \mathbf{P}^{kj}\cdot\left(\mathbf{v}^k - \mathbf{v}^j\right) + \boldsymbol{\omega}^k \times \mathbf{r}^{kj} + \boldsymbol{\omega}^j \times \mathbf{r}^{jk}. \tag{2.A6}$$

Its magnitude is denoted by $s^{kj} = \left|\mathbf{s}^{kj}\right|$, so that the unit tangential vector is $\mathbf{t}^{kj} = \mathbf{s}^{kj}\big/s^{kj}$.

The magnitude of the tangential force is modeled as viscous regularization of the Coulomb law, with the characteristic velocity v_R (2.3):

$$f_t^{kj} = \mu f_n^{kj} \left(\frac{s^{kj}}{v_R} \right)^{1/c} \tag{2.A7}$$

where μ is the coefficient of friction and c is a large number.

Appendix B

For a 2D problem, the quasistatic coefficient ϕ, and the size coefficient ψ are given by

$$\phi = \frac{mv_0}{f_0 t_0}(2N)^{1/2}, \quad \psi = 2R/L = (2N)^{-1/2}. \tag{2.B1}$$

For the present simulations, the particles are assigned the material constants of quartz. The elastic plane strain modulus of the material is 16.4835×10^9GPa , and the coefficient of inter-particle friction is assumed to be 0.45. The plate is assumed to be of the same material. The assembly consists of particles with uniform size distribution 0.5 – 1.0 mm, giving the average radius of 0.75 mm. The confining pressure is 10^5 N/m^2 , and the compressive axial strain of 10% is imposed in a simulation time of 20 sec, giving an imposed nominal strain rate $\dot{\varepsilon}_0 = 0.005$ s^{-1}, and the characteristic time $t_0 = 1/\dot{\varepsilon}_0 = 200$ s .

The mass density of the material is taken to be 2.765×10^8 kg/m^3 , which is 10^5 times the actual mass density of quartz. Using the coefficient of contact damping of 0.002 s, the appropriate large time step (Δt) was found to be 10^{-5} s .

Two different assemblies of size 983 and 3970 particles were simulated. For the 983 disk assembly, the externally imposed velocity and the relative velocity of neighboring particles are,

$$v_0 = \dot{\varepsilon}_0 L/2 = 0.18 \text{ mm s}^{-1}, \quad v_R = 2\dot{\varepsilon}_0 R = 7.5\times10^{-3} \text{ mm s}^{-1} \tag{2.B2}$$

The quasistatic coefficient and the size coefficient are computed as

$$\phi = 1.1748\times10^{-4}, \quad \psi = 0.021 \approx 1/50. \tag{2.B3}$$

References

1. Drescher A & DeJosselin DeJong G. Photoelastic verification of a mechanical model for the flow of a granular material. *Journal of the Mechanics and Physics of Solids* 1972; 20: 337-351.
2. Oda M & Kazama H. Microstructure of shear bands and its relation to the mechanisms of dilatancy and failure of dense granular soils. *Geotechnique* 1998; 48(4), pp. 465-481.
3. Alshibli KA, Batiste SN, Sture, S. Strain localization in sand: Plane strain versus triaxial compression. *Journal of Geotechnical and Geoenvironmental Engineering* 2003; 129(6), pp. 483-494.
4. Alshibli KA & Sture S. Shear Band Formation in Plane Strain Experiments of Sand. *Journal of Geotechnical and Geoenvironmental Engineering* 2000; 126(6), pp. 495-503.
5. Finno RJ, Harris WW, Mooney MA, Viggiani G. Shear bands in plane strain compression of loose sand. *Geotechnique* 1997; 47(1), pp. 149-165.
6. Parhami F and McMeeking RM. A network model for initial stage sintering. *Mechanics of Materials* 1998; 27: 111-124.
7. Cundall PA. & Strack ODL. A discrete numerical model for granular assemblies. *Geotechnique* 1979; 29(1), pp. 47-65.
8. Martin CL, Bouvard D, Shima S. Study of particle rearrangement during powder compaction by the Discrete Element Method, *Journal of the Mechanics and Physics of Solids* 2003; 51: 667 – 693.
9. Thornton C & Antony SJ. Quasi-static shear deformation of a soft particle system, *Powder Technology* 2000; 109: 179–191.

10. Thornton C & Antony SJ. Quasi-static deformation of particulate media, *Philosophical Transactions of the Royal Society A* 1998, 356: 2763–2782.
11. Bardet JP. & Proubet J. Adaptive dynamic relaxation for statics of granular materials, *Computers & Structures* 1991; 39(3/4), pp. 221-229.
12. Gear CW and Kevrekidis IG. Constraint-defined manifolds: A legacy code approach to low-dimensional computation. *Journal of Scientific Computing* 2005; 25 (1-2), pp. 17 - 28. DOI 10.1007/BF02728980
13. GDR MiDi. On dense granular flows. *The European Physical Journal E* 2004; 14: 341 - 365.
14. Hu N & Molinari JF. Shear bands in dense metallic granular materials. *Journal of the Mechanics and Physics of Solids* 2004; 52: 499-531.
15. Brilliantov NV, Spahn F, Hertzsch JM and Poschel T. Model for collisions in granular gases. *Physical Review E* 1996; 53 (5), pp. 5382 – 5392.
16. Jodrey WS and Tory EM. Simulation of random packing of spheres. *Simulation* 1979; 32 (1), pp. 1-12.
17. Bagi K. Stress and strain in granular assemblies. *Mechanics of Materials* 1996; 22: 165-177.
18. Satake M. Tensorial form definitions of discrete-mechanical quantities for granular assemblies. *International Journal of Solids and Structures* 2004; 41 (21), pp. 5775–5791.
19. Christoffersen J, Mehrabadi MM & Nemat-Nasser S, A micromechanical description of granular material behavior. *ASME Journal of Applied Mechanics* 1981; 48: 339-344.
20. Mesarovic S. Dj and Padbidri J. Minimal kinematic boundary conditions for simulations of disordered microstructures. *Philosophical Magazine* 2005; 85 (1), pp. 65-78.
21. Mesarovic S. Dj and Padbidri J. Transition between the models in multiscale simulations: Continuum and network models. *Proc. CP973*, *Multiscale and Functionally Graded*

Materials 2006, Edited by G. H. Paulino, M.-J. Pindera, R. H. Dodds, Jr., F. A. Rochinha, E. V. Dave, and L. Chen, p. 171-177. 2008 American Institute of Physics 978-0-7354-0492-2/08/. http://proceedings.aip.org/proceedings/cpcr.jsp

22. Padbidri JM. and Mesarovic S.Dj. 2010 Manuscript in preparation.

23. Schofield A and Wroth P. Critical *State Soil Mechanics*. McGraw-Hill, London 1968.

3. The effect of boundary conditions on the deformation of granular material

3.1 Introduction

Granular materials are one of the most complex and commonly found class of materials in nature whose realm of significance includes earthquake engineering, powder metallurgy, and pharmaceuticals which renders understanding their rheological behavior important. Granular media exhibit a set of complex behaviors, which separates them from conventional engineering materials, like dilatancy and almost always, strain localization in the form of shear bands.

Preliminary experimental studies [1] revealed the inherent load bearing inhomogeneity in this class of materials through the formation of force chains. The above studies reveal that though the force chains are non-uniform, they are structured. Recent advances in using X-ray based studies [2, 3] have shed light on the typical behavior of granular materials. In particular, Oda and Kazama [2] observed the creation of voids and increased particle rotations associated with the formation of shear bands. Despite the insights provided, experiments are limited in terms of reproducibility and frequency of data extraction.

Computational methods such as the discrete element method, proposed by Cundall and Strack [4] overcome this handicap. The method (DEM) employs a method very similar to molecular dynamics by treating each particle as an independent entity and integrating its Newtonian equations of motion subject to contact and boundary forces and moments. The particles are assumed to be rigid with soft contacts i.e. overlap of two particles at the point of contact is allowed, but the particles are assumed to retain their shape, a simplification intended for computational ease. The DEM has been instrumental in revealing the micromechanics

involved with the formation of shear bands, especially the instability of force chains and the high rotations of particles [5]. Though not presented in this publication, the authors confirm the high rotations associated with strain localization in granular materials. However, the effect of the boundary conditions in inducing these instabilities has never been explored primarily due to the lack of alternative boundary conditions to the conventional triaxial tests.

This article introduces the Minimal boundary conditions for granular materials which impose strain without the boundary rigidity associated with traditional experiments. A brief review of the computational procedures associated with the existing boundary conditions followed by the development of the minimal conditions is presented in section 3.2. The assembly setup is discussed in section 3.3. The results and comparison are presented in section 3.4 followed by the conclusions.

3.2 Boundary conditions

The most common experimental method employed by geomechanicians to study the behavior of granular materials is the triaxial compression. The apparatus confines the granular material in a flexible membrane subject to a confining pressure in the lateral direction and strain is imposed in the axial direction using rigid plates. Numerous researchers have implemented the experiment computationally for biaxial [6 – 8] and triaxial cases [9 – 11].

Two approaches are commonly used for prescribing the boundary conditions for a biaxial test. While the strain is imposed using a set of rigid plates in the axial direction, the definitions of the lateral boundary to impose the confining pressure differ. The confining pressure may be applied by prescribing an additional set of frictionless particles to simulate the membrane used in

experiments [7, 10 & 11]. Typically, the size of the particles prescribed in the membrane is larger than the average size of particles of the assembly to prevent particles from the assembly escaping the confines of the membrane. This method is fairly simple in the computational sense as no updates need be performed on the particles forming the membrane other than time integration of their positions along with the rest of the assembly. The other method is to identify a set of particles which form the lateral boundary and impose pressure directly on them as forces [6 & 9]. As the deformation progresses, the set of particles forming the lateral boundary changes and is updated continuously increasing the computational complexity. A schematic of both the cases is shown in figure 3.1.

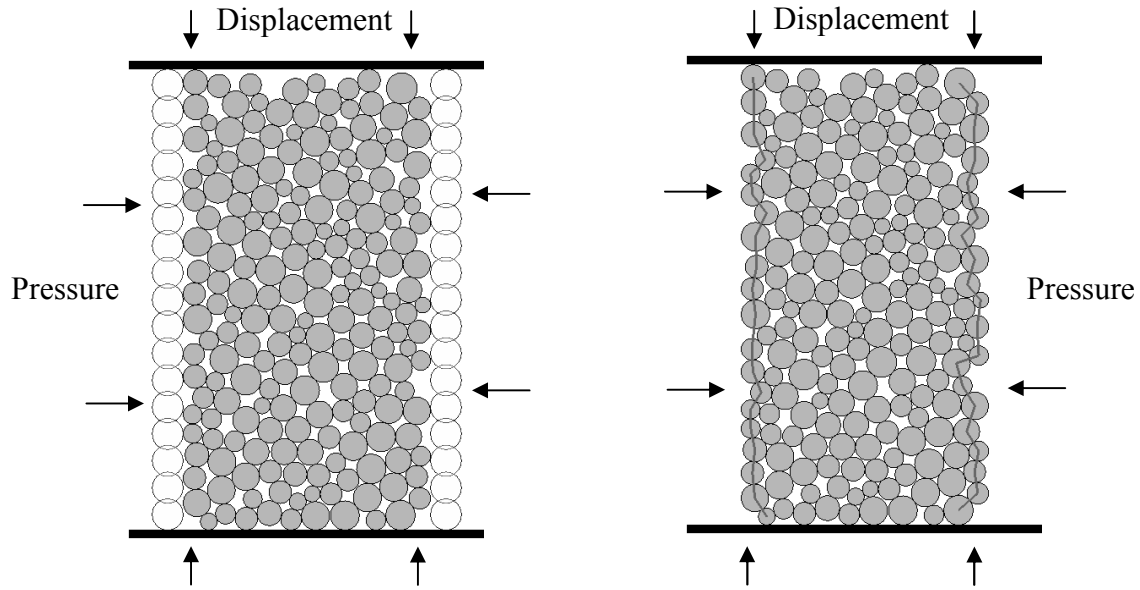

Figure 3.1. Schematic of typically used boundary conditions.

The most direct way to impose strain on the assembly is by prescribing displacements/ velocities of the rigid plates in the axial direction. Despite relevance to the experimental procedure and computational ease, the use of rigid plates to impose strain is the reason for many of the properties that granular materials exhibit, like dilatancy and percolating shear. Thus the

behavior of granular material depends on the boundary conditions used. To avoid ambiguity of the effect of boundary conditions on the micromechanics of granular material, other boundary conditions have to be considered.

One possibility is the use of periodic boundary conditions [12]. However, periodic BC (i) introduce superficial cell-size wavelengths in the solution fields, (ii) allow localization only on specific planes, and, (iii) prevent response with higher order gradients [13] which is to be expected in an inhomogenous medium like granular materials i.e. the boundary conditions are too stringent for the actual micromechanics of the material to evolve. As a solution, we impose minimal boundary conditions (MBC) which impose only the strain/strain rate but no other constraint on the assembly. Kinematic MBC for fine scale continua have been implemented into the finite element framework [13]. The conditions are based on the definition of the coarse strain, as the average of the microscopic strain field, $\boldsymbol{\varepsilon}(\mathbf{x})$ over the volume V as

$$\mathbf{E} = \frac{1}{V}\int_V \boldsymbol{\varepsilon}(\mathbf{x})\, dV = \frac{1}{2V}\int_S (\mathbf{un} + \mathbf{un}) dS \tag{3.1}$$

where $\mathbf{u}(\mathbf{x})$ is the displacement vector, and $\mathbf{n}$ is the unit normal to the surface S. Compared to Periodic BC, the MBC are more accurate in predicting material behaviour [13]. Here, the application of continuum fields to discrete particle models like granular materials is addressed.

Application of such boundary conditions necessitates a continuum description of the material kinematics. The main vehicle for this will be the geometric description of the granular assembly in terms of the Delaunay graph which is the set of lines that connects the centers of the nearest neighbors and is the complementary graph to the Dirichlet (or Voronoi) tessellation graph. To create an equivalent fine-scale continuum for granular statics, we use the cell based description of granular deformation, based on Bagi's [14] and Satake's [15] kinematics. This description defines the material in terms of cells which are simplexes (triangles in 2D and

tetrahedra in 3D) where the vertices are the centers of particles and the edges connect the nearest neighbors. The physical contacts between particles, as a definition, are a subset of the set of edges of the Delaunay graph. The displacements of particles in a simplex are interpolated linearly along the edges of that simplex which forms the basis for the definition of strain for that simplex. Further, the stress for a granular material defined based on contact forces [16] is the work conjugate for the strain rate of the simplex. Thus, the cell representation defines an equivalent C° continuum whose kinematics is derived from the discrete particle displacements and is equivalent to a set of constant strain finite elements (CSFE). Thus, the implementation for quasistatic formulation of discrete element method is identical to the one in Mesarovic and Padbidri [13]. The ability to define an effective continuum also serves the purpose of rendering the confining pressure on the lateral boundary as tractions.

For dynamic, explicit integration models, such as those used for granular materials and atoms, the additional challenge is efficient implementation, not only of Delaunay construction and boundary detection, but also of prescribing the boundary conditions as displacements/forces. The DEM uses time-integration of Newtonian equations of motion with updated forces. This structure enables efficient parallelization and should be preserved. A direct implementation of integral MBC (3.1, 3.4) would introduce couple all the degrees of freedom on the boundary. While this approach would be suitable for implicit integration models such as finite elements, graph based continuum description of granular materials would require solving a system of equations for every time increment and would result in inefficient computations. Hence, an indirect implementation through the penalty method seems more appropriate. The penalty is imposed on the violation of the prescribed strain rate rather than strain. Let the prescribed strain

rate be $\dot{\mathbf{E}}_0$. At each time step, the actual strain rate will be different. The error can be expressed from (3.1) as

$$\Delta\dot{\mathbf{E}} = \frac{1}{2V}\int_S \left(\mathbf{vn} + \mathbf{nv}\right) dS - \dot{\mathbf{E}}_0 \tag{3.2}$$

where **v** is the velocity of the particle on the boundary.

Since the granular assembly can be represented by constant strain finite elements, (3.2) takes the form

$$\Delta\dot{\mathbf{E}} = \frac{1}{2V}\sum_A \mathbf{v}^A \mathbf{n} \int \psi^A - \dot{\mathbf{E}}_0 \tag{3.3}$$

Where A is a particle on the boundary, $\mathbf{v}^A$ is its velocity, ψ^A is the value of the interpolation function and **n** is the unit outward normal as shown in Figure 3.2. It is to be noted that each particle (node) A has two neighbouring nodes.

Define a convex penalty functional, the simplest form is quadratic, as

$$\Phi\left(\mathbf{v}\right) = \frac{1}{2} K \left(\Delta\dot{\mathbf{E}} : \Delta\dot{\mathbf{E}}\right) \tag{3.4}$$

The corrective (penalty) force applied to the boundary particle A is then

$$\mathbf{F}^A = -\frac{\partial\Phi}{\partial\mathbf{v}^A} \tag{3.5}$$

The summation in (3.5) is over all the particles that A is connected to on the boundary (2 in 2D). The relevant interpolation functions are shown in figure 3.2 for one of the boundary contacts.

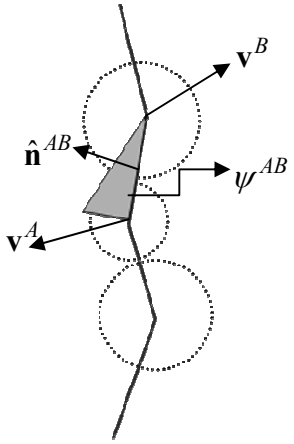

Figure 3.2. Finite element representation of the boundary.

The value of the constant K is arbitrary and its magnitude can be prescribed so the corrective forces are of the same order of magnitude as the inter-particle forces. By choosing a suitable value for K, a uniform strain rate can be obtained throughout the deformation process. The ratio of the actual strain rate to the macroscopically imposed strain rate for a case of axial compression is shown in figure 3.3.

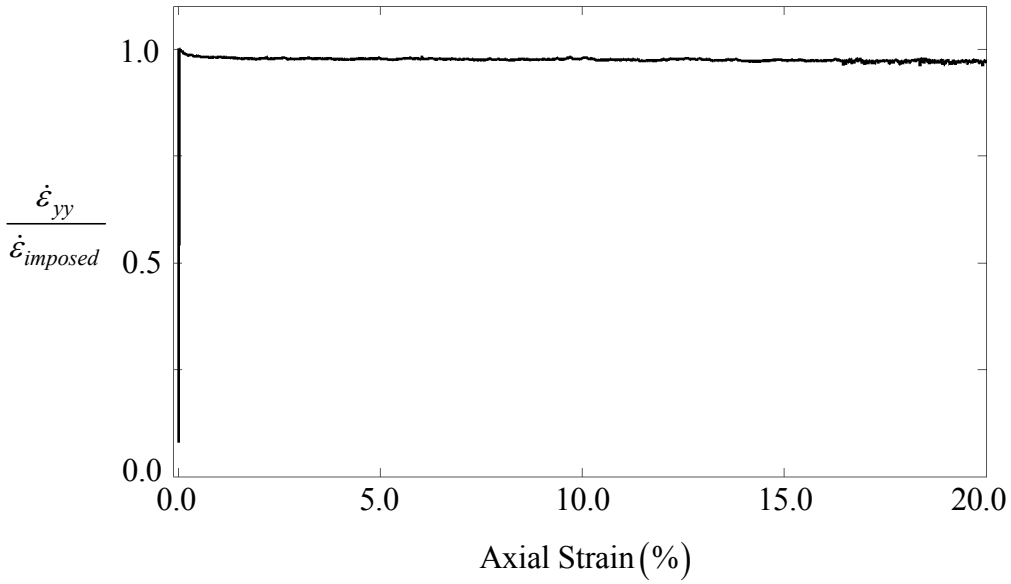

Figure 3.3. Ratio of actual and imposed macroscopic strain rates as the deformation progresses.

Owing to their integral nature, the boundary conditions can be used to apply any component of strain to any shape of computational cell. A circular computational cell subjected to shear strain is shown in figure 3.4.

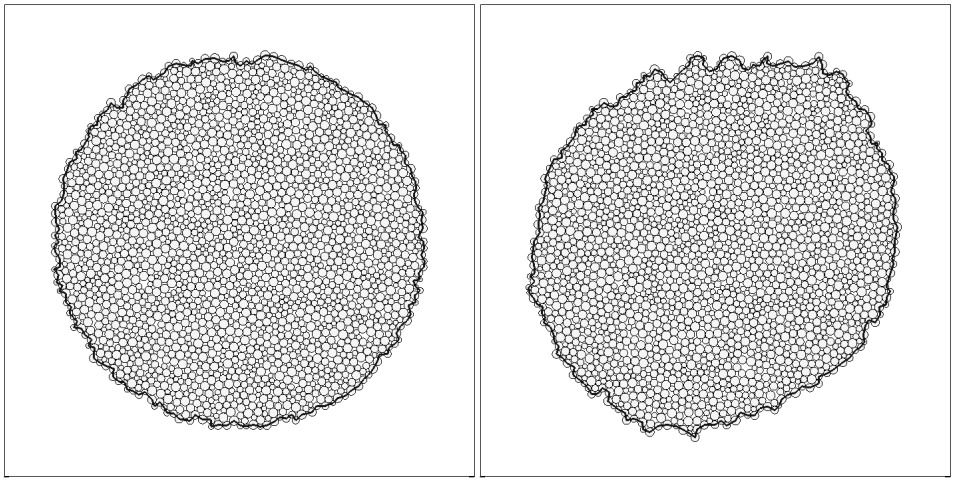

Figure 3.4. Circular assembly after 20% shear strain.

3.3 Sample preparation.

The assembly considered for the simulations is shown in figure 3.5. The initial packing is obtained by following the algorithm proposed by Jodrey and Tory [17] in which each particle is driven by gravity into a box and is allowed to rest only when it reaches a stable three contact configuration. The exceptions are the bottom layer of particles which are randomly generated to form a bed. The radii of the particles are uniformly distributed from 0.5 mm to 1.0 mm and the radii of successive particles are chosen randomly. This assembly is then subjected to lateral pressure which is slowly ramped to the value of the confining pressure. The pressure manifests as tractions on the boundary/membrane particles, as discussed previously.

After the pressure has been ramped, strain is imposed for all the three cases – by moving the plates for the membrane and direct pressure cases and by penalty force for the MBC. It is to

be noted that strain is imposed for the direct pressure and the MBC case from the same configuration in order to highlight the difference between the two. The direct pressure and the MBC cases differ in the manner in which strain is imposed. For the MBC, when the strain imposition begins, the boundaries in the axial direction change from rigid plates to direct pressure on all sides. The penalty forces are imposed in addition to the forces due to the confining pressure. The particles of the membrane immediately adjacent to the plates are constrained to move vertically with the plates. No restriction is imposed on their horizontal motion or on any other degrees of freedom of the remaining membrane particles.

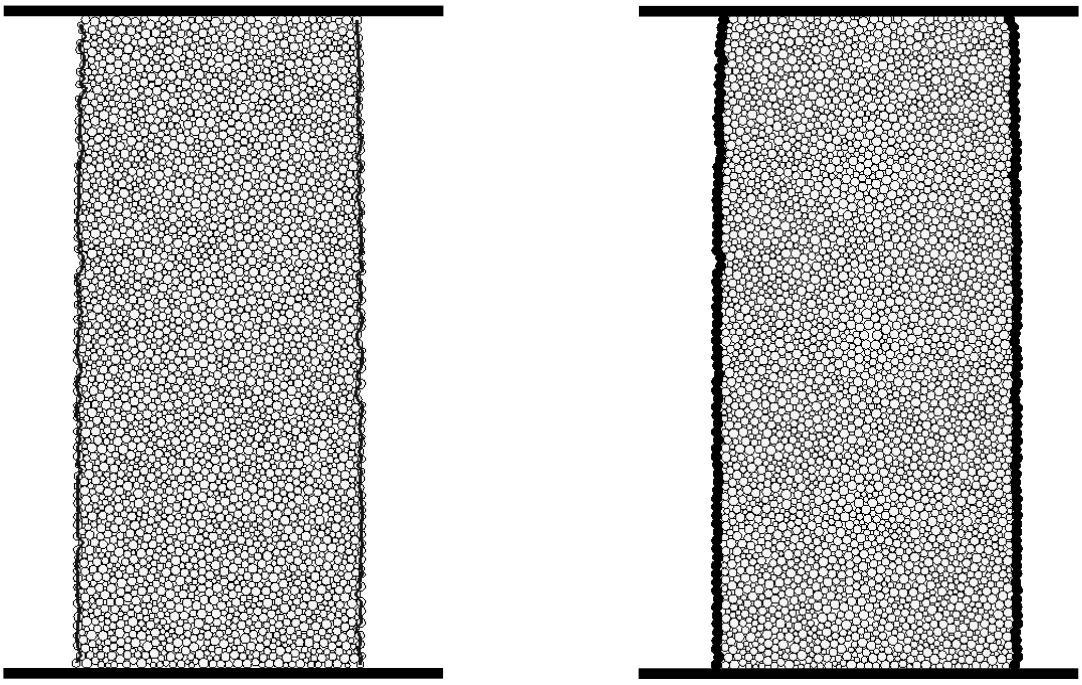

Figure 3.5. Initial configurations for the direct pressure/MBC and membrane boundary conditions. The membrane (right) is indicated by the dark set of particles.

The density of the particles are scaled by few orders of magnitude as is commonly used in DEM [18 & 19]. The deformation parameters are chosen to obtain a low value of the quasistatic coefficient (even after the mass scaling) suggested by Padbidri and Mesarovic [20]. In the same tone, a two-timescales algorithm is used for the time integration of positions and

velocities of the particles based on the concept of inertial manifolds by Gear and Kevrekedis [21]. The assemblies are subject to 20% compressive strain. Following the convention used in geomechanics, compressive strain is treated to be positive. The material constants and simulation parameters are provided in Table 3.1 in the appendix.

3.4 Results and discussion

Strain localization in the form of shear bands is one of the most characteristic behaviors of granular materials. In the present case (low confining pressure) the imposed strain manifests on a microscopic scale in the form of particle rearrangement, not individual particle deformation. The confining pressure used is low such that the assembly lies below the critical line in the $p - v$ space at the beginning of compression. Thus one would expect dilation as the deformation progresses. The change in volumetric strain as the axial strain is imposed is shown in figure 6. The volumetric strain is computed from the strain rate components defined using Bagi's definitions and integrating them with time. The quantities defined over the volume reduce to an integral (summation) over the boundary (3.2).

It is seen that both cases where strain is imposed using rigid plates, viz. direct pressure on the particles and prescribing a membrane, produce macroscopic dilation while the minimal boundary conditions do not. Typically in a biaxial/triaxial test, the shear band forms at the peak of the volumetric strain curve and as the shear band propagates, a dip in the volumetric strain is observed. For both the direct pressure and membrane boundary conditions, the volumetric strain peaks at approximately the same time (~ 12% strain). In contrast, the MBC exhibits two distinguishable characteristics: 1) the assembly does not show any macroscopic dilation meaning

it is in compression throughout the deformation and 2) the volumetric strain curve exhibits local peaks (~ 12%, 16% strain) indicating that there is strain localization that is neither observable on the macroscopic scale nor persistent.

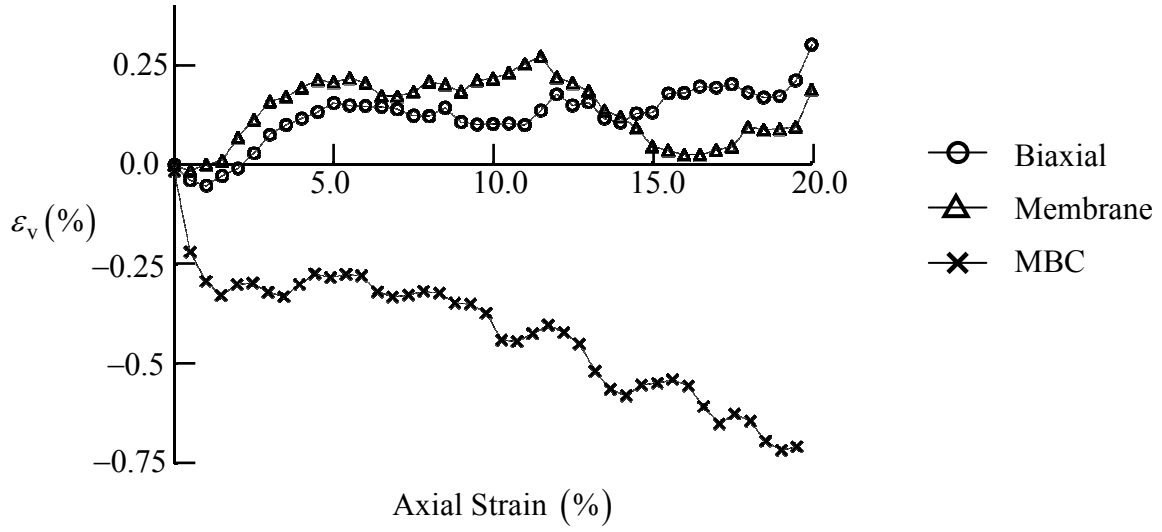

Figure 3.6. Evolution of volumetric strain with imposed axial strain

The details of strain localization are best observed by plotting the trajectories of all the particles. The displacement plots of the assemblies through relevant strain windows are shown in figures 3.7, 3.8 and 3.9. The plots (fig.s 3.7(a) and 3.8(a)) demonstrate the formation of a shear band when rigid plates are used to impose strain. The localization begins to occur at about 12% strain for both direct pressure and membrane boundaries corresponding to a peak in the volumetric strain. The displacement trajectories in a subsequent strain window are shown in figures3. 7(b) and 3.8(b). The localization that began in the previous strain window is seen to intensify and form a well defined shear band. Correspondingly, the volumetric strain drops. However, for the minimal boundaries, figure 3.9 depicts non-persistent shear localization. As seen in figure 3.9(a), localization does begin to form, but is not propagated through the

subsequent strain window. This, we believe, is the most fundamental effect of the boundary conditions. Strain is localized in granular materials due to local instabilities of the contact/force network. Imposing strain using rigid plates induces failure of force network irrespective of the local instabilities, whereas the minimal BCs do not have any such effects. The assembly deforms purely by virtue of the stability of the force networks. Consequently, persistent and percolating strain localization is rarely observed. The deformation progresses primarily through slip bands, which are intermittent and local, also observed by Kuhn [12] using periodic boundary conditions. The underlying mechanism for such behavior operates on a length scale corresponding to clusters of particles and can be explained as follows. As a slip band emerges and propagates, it runs into a portion of the assembly where the force network is stable that prevents the slip band from becoming a dominant shear band. From figures 3.7 and 3.8, it is seen that the strain localization is more obvious in the case of direct pressure boundaries compared to the membrane boundaries. The stiffness of the membrane affects the micromechanics of the assembly, especially post strain localization.

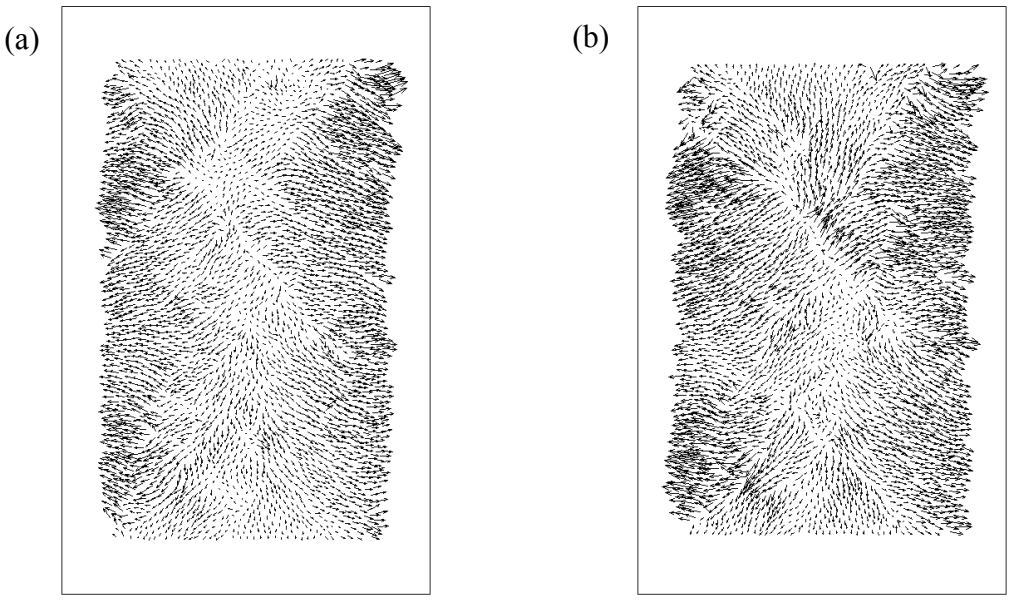

Figure 3.7. Displacement vectors relative to the affine displacement with uniform ε_{yy}, for (a) 10 – 12% strain and (b) 12 – 14% strain with pressure directly imposed on the particles

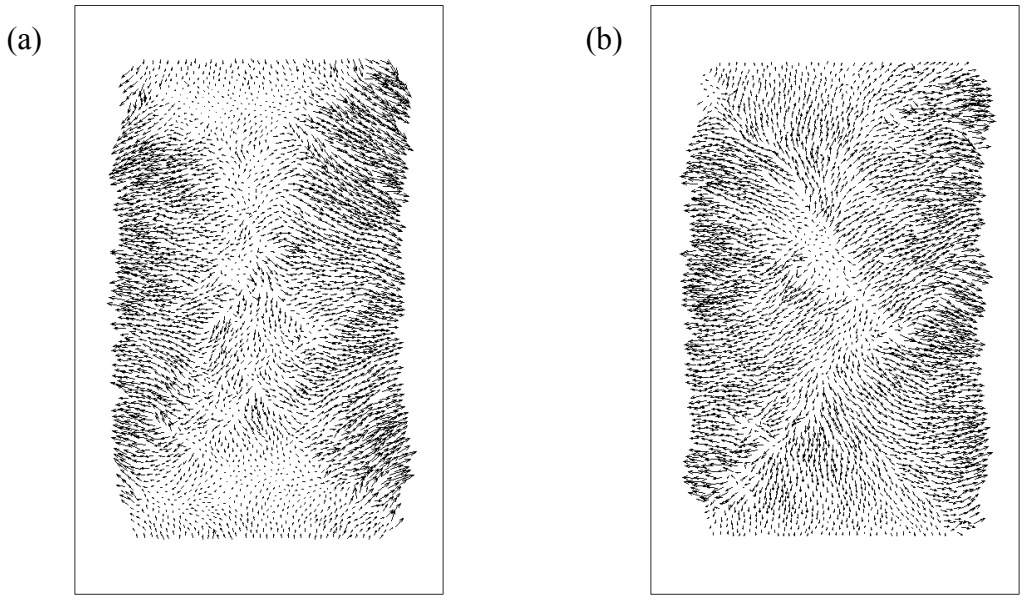

Figure 3.8. Displacement vectors relative to the affine displacement with uniform ε_{yy}, for (a) 10 – 11.5% strain and (b) 11.5 – 13.5% strain with a membrane on the lateral sides

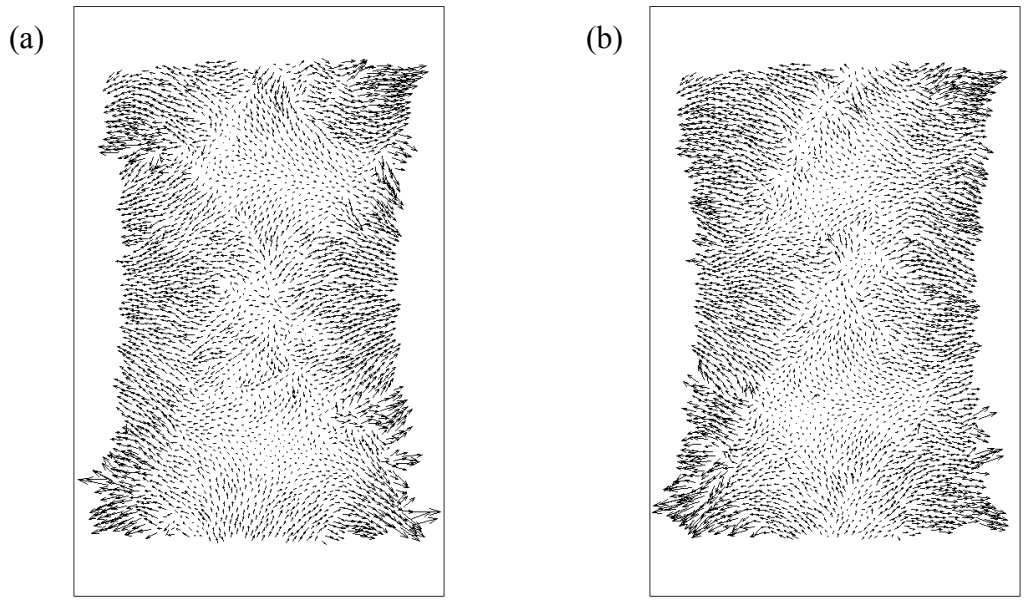

Figure 3.9. Displacement vectors relative to the affine displacement with uniform ε_{yy}, for (a) 12 – 14% strain and (b) 14 – 15.5% strain with Minimal BC

In order to further examine the effects caused by the boundary conditions, we study the distribution of deformation parameters. A very indicative parameter is the second invariant of the velocity gradient tensor (L_{II}) which represents the rate of distortion. This quantity can be found for each cell of the Delaunay graph and is plotted for the different boundary conditions in figure 3.10. The plots refer to instants of time before the shear bands shown in figures 3.7, 3.8 & 3.9 emerge. Boundaries have been added on all sides in figures 3.10 and 3.11 purely to depict the limits of the assemblies. The rigid plates used in the direct pressure and membrane boundaries (figures 3.10 (a) & (b)) cause the material near the plates to move as opposing rigid wedges (plates forming the base of the wedges) where there is very little deformation. This effectively forces the localization of strain in the center of the assembly. The MBC (figure 3.10 (c)), on the other hand, display no such boundary effects and the deformation is distributed more randomly than the other cases. Also, the MBC facilitates deformation across the axial boundary, which can never be expected with the use of rigid plates.

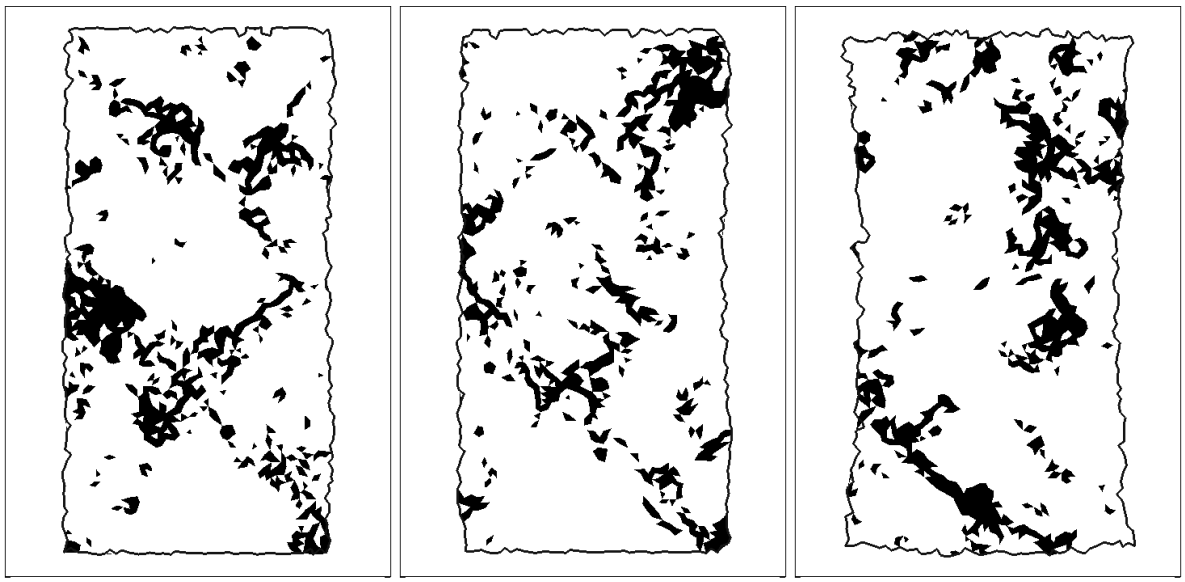

(a) (b) (c)

Figure 3.10. L_{II} plots for the (a) direct pressure boundary at 7.0% strain, (b) membrane boundary at 7.5% strain and (c) MBC at 8.5% strain. Cells are shaded for $L_{II} > 2\langle L_{II} \rangle$.

The consequence of the 'wedge effect' of the rigid boundaries is the concentration of stronger force chains and higher stresses near the plates. The first invariant of stress tensor, or the hydrostatic pressure $\left(p=\left(\sigma_{xx}+\sigma_{yy}\right)/2\right)$ for the assemblies is plotted in figure 3.11. Both cases where rigid plates have been used (figures 3.11(a) & (b)) show higher stress concentrations near the extremities of the assembly whereas the stresses are more evenly distributed for the MBC (figure 3.11(c)). Also, the membrane boundaries (figure 3.11(b)) show higher stress concentrations near the lateral boundary which is an effect of the stiffness of the membrane.

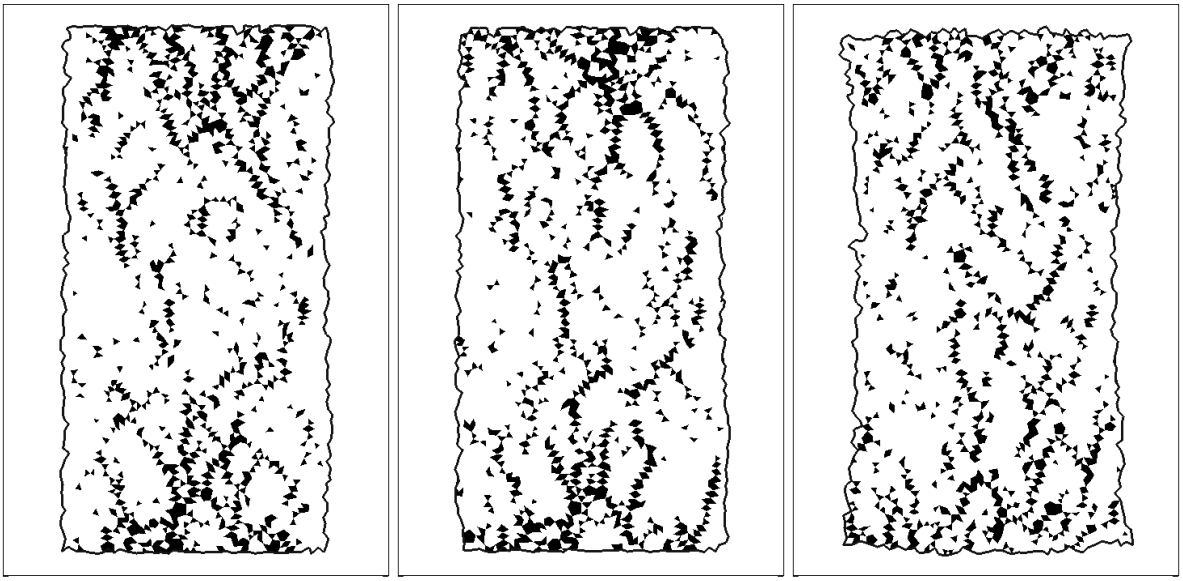

(a) (b) (c)

Figure 3.11. p plots for the (a) direct pressure boundary at 7.0% strain, (b) membrane boundary at 7.5% strain and (c) MBC at 8.5% strain. Cells are shaded for $p>1.75\langle p\rangle$.

To quantify the stress gradients caused by the rigid plates, we consider the evolution of the average pressure for clusters of particles. We define circles of increasing diameters at different places in the assembly viz. near the top plate, center and near the bottom plate. The ratio of average pressure of all Delaunay cells within this circle $\left(p_{circle}\right)$ and the average pressure of the assembly as the size of the circle changes is plotted in figure 12. The diameter of the

circle is denoted by d_{circle} and the average diameter of the particles in the assembly is d. The horizontal lines in figure 3.12 represent the average pressure of the entire assembly. While both the direct pressure and the MBC display higher average pressure at the axial extremities of the assembly, the variations of the pressure for the MBC (figure 3.12(b)) are lower than for the direct pressure boundaries (figure 3.12(a)). Also, the pressure for the MBC converges faster to the assembly average as the size of the cluster increases.

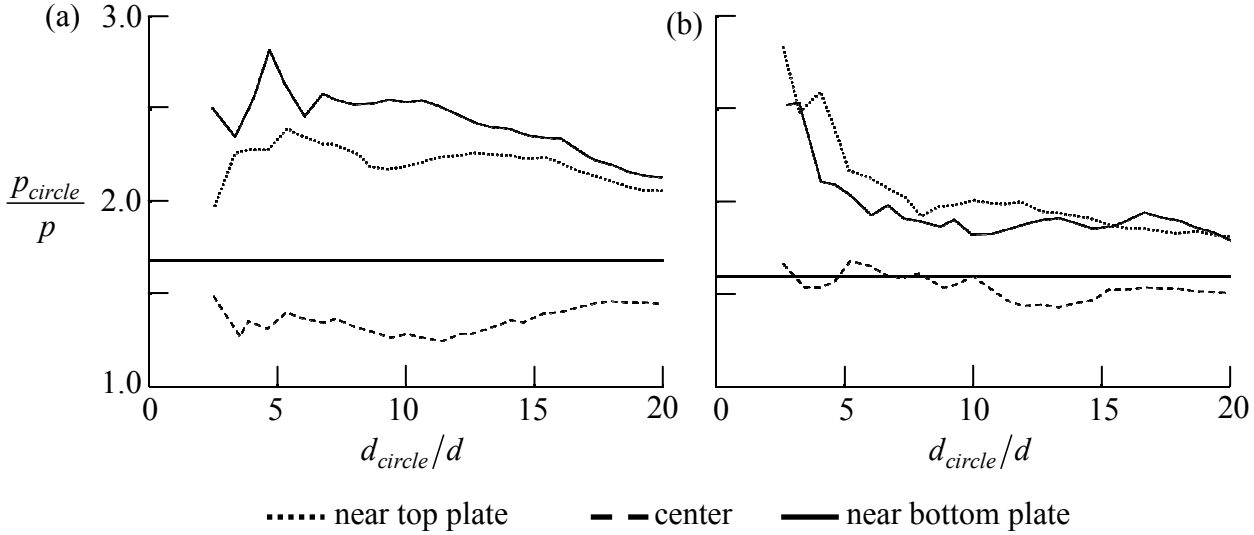

Figure 3.12. Variation of pressure over a cluster of particles for (a) direct pressure boundary at 7.0% strain and (b) MBC at 8.5% strain.

While the MBC impose strain without the rigidity of the boundary and promote strain localization independent of boundary effects, there is a noticeable size effect associated with the method. The deformed configurations at 10% strain of assemblies of increasing sizes are plotted in figure 3.13. The behavior of the smaller assembly (figure 3.13(a)) is similar to the results presented thus far. However, as the assembly size increases, the boundary begins to lose its shape characterized by boundary distortion at the corners. The consequence is a significant curvature of the boundary (figures 3.13(b) & (c)). Though not presented here, the primary mechanism causing this shape distortion has been identified to be excessive rolling of the

particles at the corners. Once the corners begin deforming more than the assembly, greater amount of strain concentrates there since rolling is an easier mechanism of deformation. The relation with increase in the size of the computational cell seems to indicate this behavior is associated with a cluster of particles. As the cell size increases well beyond the size of this cluster, the boundary instabilities appear. It is to be noted that similar shape distortions have been observed by other researches [22 & 23] using the MBC. These problems have been solved by FEM for which MBC offers a closed form solution. For the problem on hand, however, DEM does not facilitate unique solutions for the entire computational cell. Imposing a stricter constraint on the shape of the boundary without any implicitly associated rigidity remains an open question.

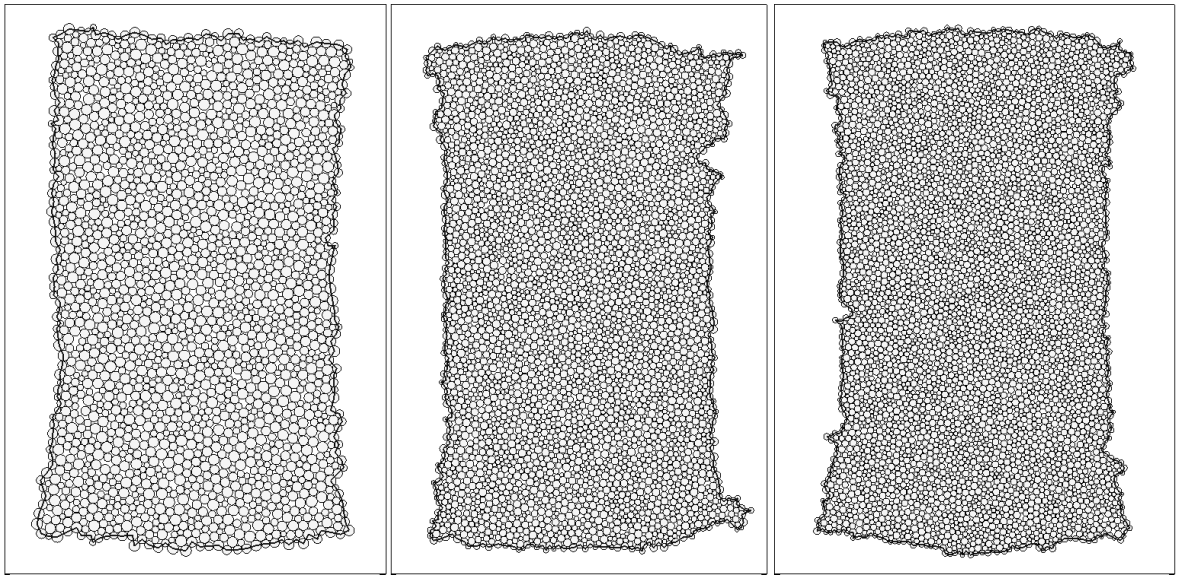

(a) (b) (c)

Figure 3.13. Size effects of MBC. Deformed configurations at 10% strain for an assembly of (a) 2100 particles, (b) 3970 particles and (c) 5034 particles.

3.5 Conclusions

Minimal boundary conditions for discrete particles with contact forces have been developed based on the equivalent definitions of continuum using the Delaunay graph. Biaxial

compression has been simulated using three boundary conditions on an assembly of particles. The commonly used method of imposing strain using rigid plates is shown to produce macroscopic dilation and percolating shear bands. The dominant shear bands are the result of near rigid body motion of a sizeable section of the assembly near the plates. The use of membranes to prescribe an artificial lateral boundary affects the micromechanics and the distribution of stresses. The minimal boundary conditions do not produce macroscopic dilation. However, they do produce intermittent, non-percolating slip bands and allow strain localization across the axial boundaries. The stress gradients produced by the MBC are considerably lower than with the rigid plates method.

Acknowledgements

This research was supported in part by US DOE/MICS, Grant # DE-FG02-05ER25709.

Appendix

The normal forces at the contact are modeled using the Hertz contact model. The impact of two particles in a granular assembly is near plastic since each particle is subjected to frictional contacts with its neighbors such that most of the kinetic energy is dissipated yielding a very low coefficient of restitution. To account for this, we use a non-linear viscoelastic, stiffness proportional damping at the contacts [24]. The viscous nature of the damping implies that most of the energy is dissipated for high velocities of impact but is stored as elastic energy for slow deformation and also ensures numerical stability. Thus, the normal force is defined as

$$F_n = K_n \left(\delta\right)^{3/2} - \alpha K_n \dot{\delta} \left(\delta\right)^{1/2} \tag{3.A1}$$

Where $K_n = 4\bar{E}R^{1/2}/3$, where $\bar{E} = E/2\left(1-\nu^2\right)$ is the effective plane-strain elastic modulus, $R = r^i r^j \Big/ \left(r^i + r^j\right)$ is the effective contact radius of particles *i* and *j* and δ is the depth of indentation. The contact damping acts opposite to the change in δ and the coefficient α (<< 1) can be prescribed to obtain the desired coefficient of restitution. The magnitude of the tangential force is modeled as a viscous regularization of Coulomb's law with the characteristic relative velocity between the particles [20]. Consider an assembly of particles with average diameter d and imposed macroscopic strain rate $\dot{\varepsilon}$. The characteristic relative velocity between the particles is given by

$$v_R = d\dot{\varepsilon} \tag{3.A2}$$

The magnitude of the tangential force is prescribed as

$$F_t = \mu F_n \left(\frac{v_{slip}}{v_R}\right)^{1/m} \tag{3.A3}$$

Where μ is the coefficient of friction, v_{slip} is the net slip at the contact due to both translations and rotations and m is a large number.

Table 3.1: Material constants and simulation parameters.

Number of particles	3279
Elastic modulus of the particles	30 GPa
Poisson's ratio	0.3
Confining pressure	100 KPa
Density of the particles	2.675×10^8 Kg/m^3 (scaled up by 10^5)
Average radius of particles	0.75 mm
Time step	10^{-5} s
Strain rate	5×10^{-3} s^{-1}
Coefficient of friction	0.45
Membrane stiffness	10 N/mm

References

1. Drescher, A., DeJosselin DeJong, G., 1972. Photoelastic verification of a mechanical model for the flow of a granular material. Journal of the Mechanics and Physics of Solids. 20, 337-351.
2. Oda, M., Kazama, H., 1998. Micro-structure of shear band and its relation to the mechanism of dilatancy and failure of granular soils. Geotechnique, 48, 465–481.
3. Alshibli, K.A., Batiste, S.N., Sture, S., 2003. Strain localization in sand: plane strain versus triaxial compression. Journal of geotechnical and geoenvironmental engineering. 129, 483 – 494.
4. Cundall, P.A., Strack, O.D.L., 1979, A discrete numerical model for granular assemblies. Geotechnique. 29, 47-65.
5. Tordesillas, A., 2007. Force chain buckling**,** unjamming transitions and shear banding in dense granular assemblies. Philosophical Magazine. 87, 4987 – 5016.
6. Bardet, J.P., Proubet, J., 1991, A numerical investigation of the structure of persistent shear bands in granular media. Geotechnique. 41, 599-613.
7. Iwashita, K., Oda, M., 2000. Micro-deformation mechanism of shear banding process based on modified distinct element method. Powder Technology. 109, 192-205.
8. Hu, N. & Molinari, J.F., 2004. Shear bands in dense metallic granular materials. Journal of the Mechanics and Physics of Solids, 52, 499-531.
9. Kuhn, M.R., 1995. A flexible boundary for three-dimensional DEM particle assemblies. Engineering computations. 12, 175-183.
10. Tsunekawa, H., Iwashita, K., 2001. Numerical simulation of triaxial test using two and three dimensional DEM, in: Kishino Y. (Ed.), Powders and grains 2001: Proceedings of the Fourth

International Conference on Micromechanics of Granular Media. Taylor & Francis., 177-180.

11. Fazekas, S., Torok, J., Kertesz, J., Wolf, D.E., 2006. Morphologies of three-dimensional shear bands in granular media, Physical review E. 74, 031303-1 – 031303-6.
12. Kuhn, M.R., 1999. Structured deformation in granular materials. Mechanics of materials. 31, 407 – 429.
13. Mesarovic, S. Dj., Padbidri, J., 2005, Minimal kinematic boundary conditions for simulations of disordered microstructures. Philosophical Magazine. 85, 65-78.
14. Bagi, K., 1996. Stress and strain in granular assemblies. Mechanics of Materials. 22, 165-177.
15. Satake, M., 2004, Tensorial form definitions of discrete-mechanical quantities for granular assemblies. International Journal of Solids and Structures. 41, 5775–5791.
16. Christoffersen, J., Mehrabadi, M.M., Nemat-Nasser, S., 1981. A micromechanical description of granular material behavior. ASME Journal of Applied Mechanics. 48, 339-344.
17. Jodrey, W.S., Tory, E.M., 1979. Simulation of random packing of spheres. Simulation. 32, 1-12.
18. Thornton, C., Antony, S.J., 2000, Quasi-static shear deformation of a soft particle system. Powder Technology. 109, 179–191.
19. Martin, C.L., Bouvard, D., Shima, S., 2003, Study of particle rearrangement during powder compaction by the Discrete Element Method. Journal of the Mechanics and Physics of Solids. 51, 667 – 693.

20. Padbidri, J.M., Mesarovic, S. Dj., 2010. Acceleration of DEM algorithm for quasistatic processes. Under review, International journal of numerical methods in engineering.
21. Gear, C.W., Kevrekidis, I.G., 2005. Constraint-defined manifolds: A legacy code approach to low-dimensional computation. Journal of Scientific Computing. 25, 17 - 28.
22. Inglis, H.M., Geubelle, P.H., Matous, K., 2008. Boundary condition effects on multiscale analysis of damage localization. Philosophical magazine. 88, 2373-2397.
23. Fish, J., Fan, R., 2008. Mathematical homogenization of nonperiodic heterogeneous media subjected to large deformation transient loading. International journal for numerical methods in engineering. 76, 1044-1064.
24. Brilliantov, N.V., Spahn, F., Hertzsch, J.M., Poschel, T., 1996, Model for collisions in granular gases. Physical Review E. 53, 5382 – 5392.

4. Rotation length scales of granular materials

Note: The computations in this Chapter were performed in part by Carly M. Hansen , REU student (Summer 2009), under my supervision.

4.1 Introduction

Granular materials are composed of discrete particles of varying sizes which contribute to their inherent inhomogeneity and anisotropy. This anisotropy is strongly reflected in the way the forces are distributed in a granular material, proven by experiments using photoelastic disks [1] characterized by "strong force chains" which carry a load greater than the average applied load and "weak force chains" which carry a lesser than average load. Statistical studies [2] have quantified the distribution of force chains. It was found that the number of force chains that carry a load greater than the average decreases exponentially as the magnitude of the load increases. Though distributed unevenly, the force chains form a structure that is stable enough to bear the applied load [3]. When the stability of this force chain structure is broken, the material begins to localize strain in the form of shear bands. The extent to which the instabilities are propagated, by unjamming and jamming of clusters of particles [4] determines the length of the shear band i.e. the material might experience local instabilities which do not propagate resulting in localized slip bands [3, 5] or the instabilities percolate to create a behavior similar to an avalanche [4, 6].

Regardless of the extent to which shear bands propagate, they are characterized by increased rotation of particles [4, 6, and 7] which indicates that rolling rather than sliding is the preferred way of particle rearrangement inside a shear band. One argument presented for the

increased rotations [4, 6] is that the force chain buckles under the applied load and the buckling is initiated by the particles rolling over each other into an unstable configuration. However, sustained rotations were observed even after the shear band forms. This means that while the buckling of the force chain instigates the rotations, it is not the only mechanism that contributes to the observations. The problem warrants a detailed study of the relation between the contact network of an assembly and the transmission of rotations through it.

When a densely packed assembly deforms, zero slips at all points of contact are practically unattainable. The interconnected force network of a densely packed assembly does not allow a simple distribution of rotations. For example, consider the cluster of particles shown in figure 1. The three particles A, B and C are in contact with each other and particle A is rotating in the counter-clockwise direction. For the particles to roll over each other or even in the case when one particle drives the motion of the other, the relative slip velocity at the points of contact must be zero. This implies that both particles B and C would have to rotate in the clockwise direction under influence from particle A when each is considered individually. But if this were accomplished, the point of contact between particles B and C would experience slip, not rolling. If either B or C reacts to this slip and adjusts its angular velocity, then it would slip at the point of contact with A.

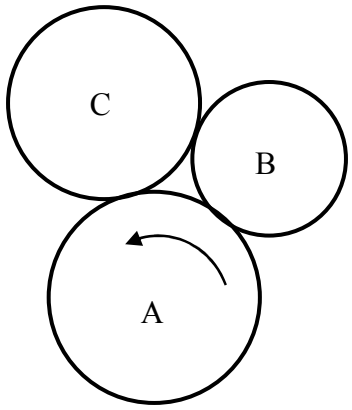

Figure 4.1. Rotation in a cluster of particles

The cluster of particles would have to react to the constraints imposed by the particles on each other so that the total slip at all the contacts is minimized. This implies that perfect rolling is not established at any contact. Thus the angular velocity of particle A is not entirely transmitted to its neighboring particles and the angular velocity decays at every point of contact. It was observed in numerical experiments [4] that the magnitude of angular velocity of a particle dies down as one progresses from the center of a shear band to its periphery. Thus, there would be a fixed distance from point A, depending on the contact network in its vicinity, beyond which the angular velocity of A will not be transmitted. This length scale could be addressed as the rotation transmission distance, which might provide insight into the distribution of angular velocities in a shear band and the width of the shear band itself.

4.2 Problem setup

For the purpose of establishing a relation between the transmission of particle rotations through the contact network of an assembly, we perform numerical experiments on an assembly of particles using the discrete element method (DEM) [8]. The DEM is a molecular dynamics based method in that each particle is considered as an independent entity and its equations of motion, subject to contact and boundary forces are integrated in time. Additional complexities are introduced in simulating a granular material due to the introduction of the additional rotational degrees of freedom.

We consider the following study. A circular assembly of disks is subject to confining pressure with pressure directly imposed on the particles and is allowed to equilibrate. The assembly, at the end of imposing the pressure, and the corresponding force network is shown in

figure 2. The thicker lines indicate higher contact forces. A disk in the assembly is slowly rotated by ramping its angular velocity to a prescribed value and then holding it constant. The distribution of the angular velocities from the particle with a prescribed angular velocity is observed in relation to the force network surrounding it. No other constraints are imposed on the particles individually. However, the rigid body rotation of the assembly is prevented by imposing a condition that the off-diagonal terms of the displacement gradient tensor be zero. Minimal boundary conditions are used to impose the corrective forces to satisfy the conditions [5].

The assembly consists of 2827 particles whose radius varies uniformly from 0.5 to 1.0 mm giving the particles an average radius of 0.75 mm. The contact forces are modeled using the nonlinear Hertz law, with stiffness proportional viscous damping to prevent oscillations of particles [9]. Contrary to the MDEM [6], we use a viscous regularization of Coulomb Friction [10] to define the tangential forces and moments on the particles. The characteristic relaxation time associated with rotations has been identified to be lower for rotations than for translations for a biaxial compression simulation [10]. Since the primary variables of interest in this study are the particle rotations, we follow a conventional single time step algorithm. The density of the material is scaled up by a few orders of magnitude to increase the time increment and computational efficiency as is commonly followed in DEM [11, 12]. The simulation parameters are listed in table 1.

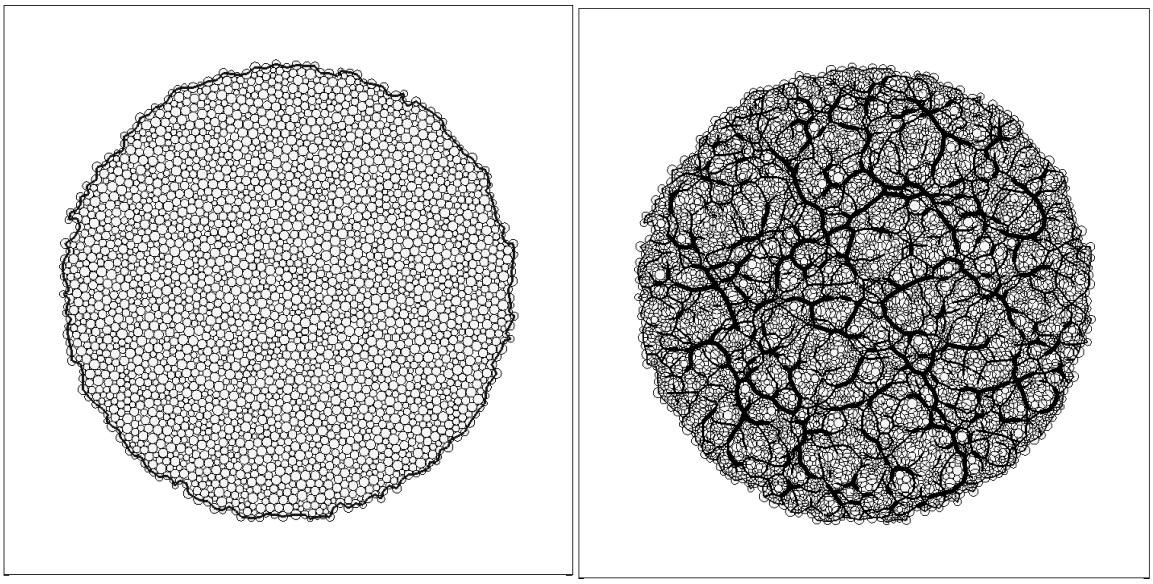

(a) (b)

Figure 4.2. (a) Assembly of disks after imposing pressure (b) Force nework of the assembly

4.3 Quantification of force chain network

The particle which is subjected to the prescribed angular velocity will be hereby referred to as the forced particle. The objective is to relate the contact network surrounding the forced particle to the propagation of rotations from it. We expect that the primary direction of rotation transmission will be radially outward from the forced particle and attempt to quantify the strength of the force network in the said direction. The most common quantity used to describe the contact network for a granular material is the fabric tensor [13]. However, the fabric tensor, defined solely using the contact normals does not take into account the strength of the force chains. Hence we propose a weighted directional tensor defined by

$$\mathbf{T} = \sum_{R} \frac{1}{|\mathbf{s}|} \hat{\mathbf{s}} \otimes \hat{\mathbf{b}} \frac{f}{\langle f \rangle} \tag{4.1}$$

Where **b** is the branch vector of an individual segment of the force chain network and **s** is the position vector of the mid-point of that force chain from the forced particle as shown in figure 3. The force carried by that force chain segment is f and the average force over all the contacts in the assembly is $\langle f \rangle$. The summation is valid over all the segments of the force network whose midpoints lie within a prescribed cutoff radius R from the forced particle. Unlike the fabric tensor, the weighted directional tensor is not inherently symmetric. However, if all the segments of the force network emerge radially from the forced particle i.e. $\mathbf{b} \parallel \mathbf{s} \ \forall \ \mathbf{b}$, the tensor **T** will be purely diagonal and purely off-diagonal if $\mathbf{b} \perp \mathbf{s} \ \forall \ \mathbf{b}$. Each segment is given a weight inversely proportional to its distance from the forced particle since the effect of the forced particle is expected to decay with distance.

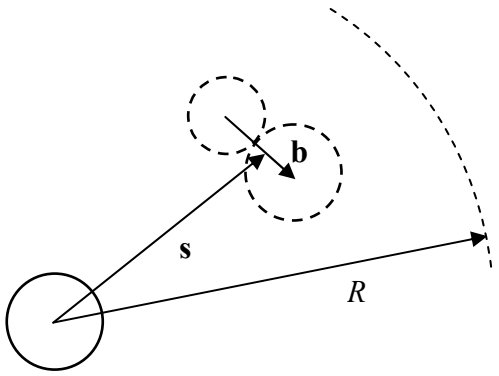

Figure 4.3. Schematic for defining the weighted directional tensor

Similarly, the contribution of an individual segment of the force network in the direction radially outward from the forced particle can be given by

$$W(\mathbf{b},\theta) = \frac{1}{|\mathbf{s}|}\hat{\mathbf{s}} \cdot \hat{\mathbf{b}} \frac{f}{\langle f \rangle} \tag{4.2}$$

which is the component of a force segment acting radially outward from the forced particle weighted with its distance from the forced particle and θ is the angle **s** makes with the horizontal.

4.4 Results and Discussion

The distribution of the magnitude of angular velocity in the vicinity of the forced particle after its velocity is ramped and held constant is shown in figure 4(a). The forced particle has been colored black. The weighted directional tensor (**T**) is calculated based on all the force chain segments within a cutoff radius of $10\langle d \rangle$ from the forced particle where $\langle d \rangle$ is the average diameter of the particles of the assembly. In the same volume of the assembly, the weighted radial component of each force chain segment $\left(W\left(\mathbf{b},\theta\right)\right)$ is found based on its position from the forced particle. The cumulative $W\left(\mathbf{b},\theta\right)$ of all the segments inside the cutoff radius for increments of θ is plotted in figure 4(b). The red lines in figure 4(b) are the directions of the Eigen vectors of the symmetric part of **T**. Both the weighted directional tensor (**T**) and the weighted radial force chain segments $\left(W\left(\mathbf{b},\theta\right)\right)$ prove to be effective in identifying strong force chains passing through the forced particle shown in figure 4(a).

From figure 4(a), it is seen that rotations propagate along strong force chains. Also, rotations are not propagated across strong force chains as observed to the bottom right of the forced particle. The most important observation is that strong force chains are not necessary for the propagation of rotations. To the top left of the forced particle, rotations propagate to a fairly appreciable distance even in the absence of a strong force chain. It is merely the absence of a force chain opposing the transmission of rotations (as to the bottom right of the forced particle) that enables the rotations to be propagated. This is of particular importance since the force

network to the top left of the forced particle is structurally similar to that in a shear band. Shear bands are characterized by failure of force networks [4, 6] so that no dominant force chain exists to either assist rotations in a specific direction or impede the transmission of rotations.

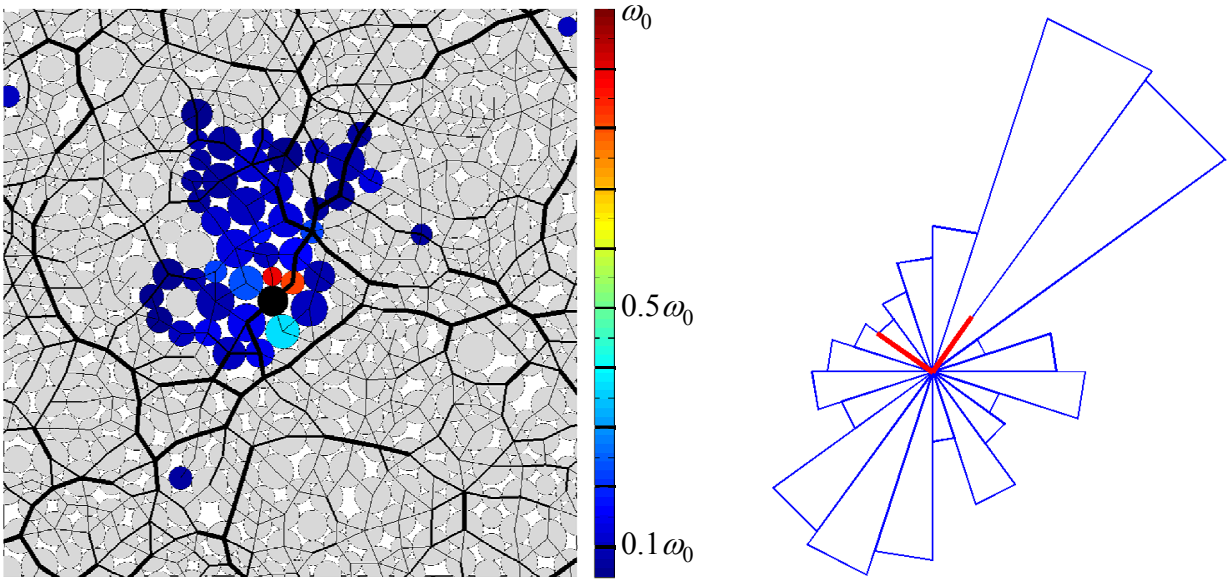

Figure 4.4. (a) Propagation of angular velocities from the forced particle (b) Rose plot of $W(\mathbf{b},\theta)$ and Eigen vectors of $Sym(\mathbf{T})$

The evolution of the magnitude of angular velocities of the particles, normalized with the prescribed velocity of the forced particle, with respect to their distance from the forced particle is plotted in figure 5. Each line in the figure corresponds to a particle in the assembly. As expected, the angular velocity decays with the distance from the forced particle. From figure 5, the effect of the forced particle can be experienced by another particle at a distance of 6 – 8 particle sizes away giving the forced particle a 'sphere of influence' of 10 – 15 particles. This length scale for rotations is the same size identified to be the width of a shear band in numerical

simulations [4]. Not surprisingly, rotations had been used to define the width of the shear band. Similar length scales have been recorded in experiments as well [7].

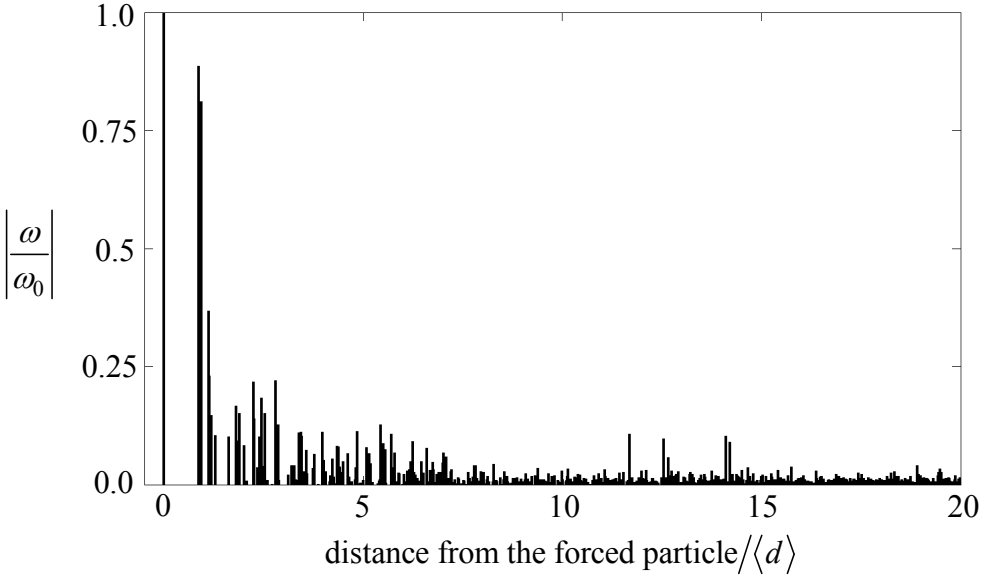

Figure 4.5. Evolution of angular velocities with distance from the forced particle

4.5 Conclusions

Numerical simulations reveal that the structure of force chains greatly affects the transmission of rotations in a densely packed granular material. Rotations propagate easily along strong force chains but not across strong force chains. The absence of such opposing force chains is the primary reason for increased rotations in a shear band. The length scale of the rotation transmission compares well with existing observations. A weighted directional tensor has been defined which approximates the distribution of contact forces based on their magnitudes.

Table 4.1: Material constants and simulation parameters.

Number of particles	2827
Elastic modulus of the particles	30 GPa
Poisson's ratio	0.3
Confining pressure	100 KPa
Density of the particles	2.675×10^8 Kg/m^3 (scaled up by 10^5)
Average radius of particles	0.75 mm
Time step	10^{-7} s
Coefficient of friction	0.45
Angular velocity prescribed (ω_0)	0.03 rad/s
Time in which the angular velocity is ramped	2.5 s

Acknowledgements

This research was supported in part by US DOE/MICS, Grant # DE-FG02-05ER25709 and the National Science Foundation's Research Experience for Undergraduates program, Grant # EEC-0754370.

References

1. Drescher A & DeJosselin DeJong G. Photoelastic verification of a mechanical model for the flow of a granular material. Journal of the Mechanics and Physics of Solids 1972; 20: 337-351.
2. Radjai F, Jean M, Moreau J-J, Roux S. Force distribution in dense two-dimensional granular systems. Physical Review Letters 1996; 77(2), pp. 274-277.
3. Kuhn MR. Structred deformation in granular materials. Mechanics of Materials 1999, 31: 407-429.
4. Tordesillas A, Force chain buckling, unjamming transitions and shear banding in dense granular assemblies. Philosophical Magazine. v 87, n 32, 4987–5016.
5. Padbidri JM. and Mesarovic S.Dj. 2010 Manuscript in preparation.
6. Iwashita K. & Oda M. Micro-deformation mechanism of shear banding process based on modified distinct element method. Powder Technology 2000; 109: 192-205.
7. Rechenmacher, A.L, 2006. Grain-scale processes governing shear band initiation and evolution in sands, Journal of the Mechanics and Physics of Solids. 54, 22–45.
8. Cundall, P.A., Strack, O.D.L., 1979, A discrete numerical model for granular assemblies. Geotechnique. 29, 47-65.
9. Brilliantov NV, Spahn F, Hertzsch JM and Poschel T. Model for collisions in granular gases. Physical Review E 1996; 53 (5), pp. 5382 – 5392.
10. Padbidri, J.M., Mesarovic, S. Dj., 2010. Acceleration of DEM algorithm for quasistatic processes. Under review, international journal of numerical methods in engineering.

11. Martin CL, Bouvard D, Shima S. Study of particle rearrangement during powder compaction by the Discrete Element Method, Journal of the Mechanics and Physics of Solids 2003; 51: 667 – 693.
12. Thornton C & Antony SJ. Quasi-static shear deformation of a soft particle system, Powder Technology 2000; 109: 179–191.
13. Satake M., 1982, Fabric tensor in granular materials. IUTAM Conference on deformation and failure of granular materials, Delft.

5. Conclusions and Future work

In this work critical questions regarding the numerical studies used for granular materials and the micromechanics of granular materials have been addressed. A dimensional analysis has been performed to determine the quasistatic nature of deformation for granular material simulations found to be dependent on the computational cell size. This is an important result since it sets bounds for the commonly used method of computational acceleration by scaling the density of the particles. The dimensional analysis of the governing equations for the particles reveals that the characteristic time of relaxation is lower for rotations of particles than for translations. To overcome this problem, a two timescales algorithm has been developed based on the concept of inertial manifolds. Different combinations for the size of the large and small time steps are used to reveal the optimum combination which guarantees accuracy with modest computational acceleration.

The effect of boundary conditions has been studied and is found to have a strong influence on the creation and propagation of fundamental deformation mechanisms in granular material. Minimal boundary conditions have been developed which impose continuum strain rate fields onto a discrete heterogeneous media like granular materials. The Minimal boundaries do not impose the boundary rigidity associated with standard biaxial tests. Consequently, deformation in the material localizes purely by virtue of the force network stability. This manifests as intermittent slip bands rather than percolating shear bands observed usually in biaxial test conditions.

Rotation length scales which are one of the fundamental parameters for granular materials have been identified. The propagation of rotations has been identified to depend strongly on the strength and orientation of the force chains.

The next step would be to extend the study to 3 dimensional configurations. The computational complexity increases enormously with the added dimension. An example of strain imposed using rigid plates and pressure imposed directly on the particles on the lateral sides is shown in figure 5.1. The evolution of the volumetric strain with the imposed axial strain is shown in figure 5.2.

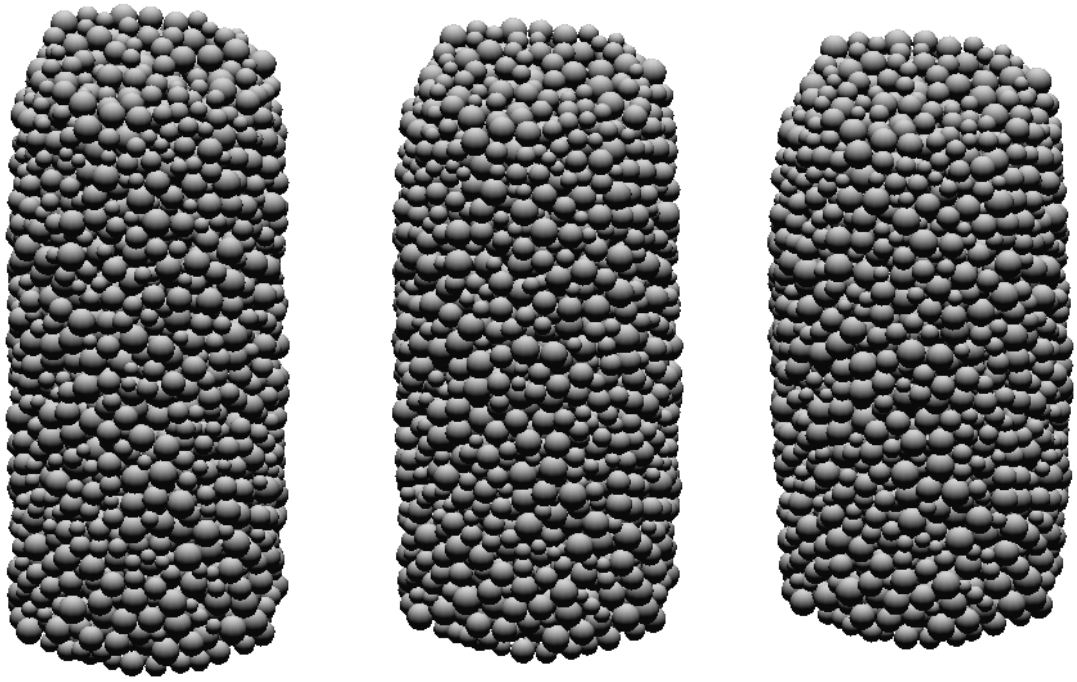

(a) (b) (c)

Figure 5.1 Assembly of 3413 spheres at (a) 0% strain (b) 5% strain and (c) 10% strain

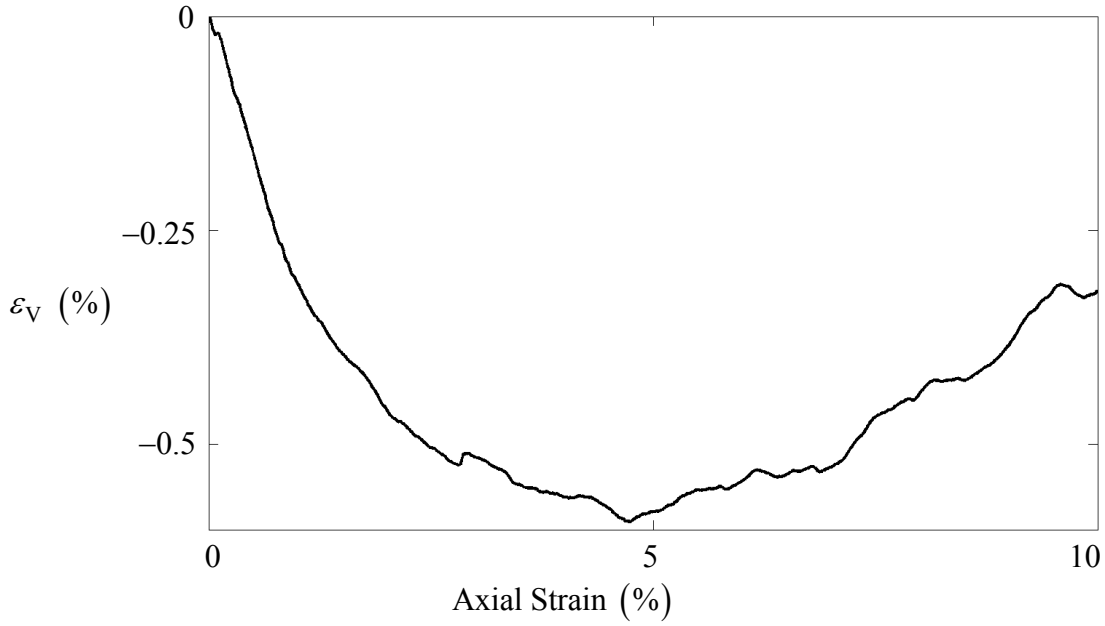

Figure 5.2 Evolution of the volumetric strain with axial strain of a 3D assembly

The representation of granular materials as a continuum is a challenging and barely understood problem. There appears to be a huge gap between the understanding particle interactions and the understanding their collective behavior. For upscaling to continuum theory, a description on the micromechanical level must be the starting point with description of connectivity of particle contacts and its evolution. In a special case when the topology of particle contacts remains unchanged, upscaling by mathematical homogenization techniques could be more successful. The critical lengths determined in this research and appropriate size of clusters of particles (figure 3.12) could be the starting points for description of a mesoscale theory.